

Quantum-Based Atomistic Simulation of Materials Properties in Transition Metals

*John A. Moriarty, James F. Belak, Robert E. Rudd,
Per Söderlind, Frederick H. Streitz, and Lin H. Yang*

This article was submitted to Journal of Physics: Condensed Matter

January 8, 2002

U.S. Department of Energy

Lawrence
Livermore
National
Laboratory

DISCLAIMER

This document was prepared as an account of work sponsored by an agency of the United States Government. Neither the United States Government nor the University of California nor any of their employees, makes any warranty, express or implied, or assumes any legal liability or responsibility for the accuracy, completeness, or usefulness of any information, apparatus, product, or process disclosed, or represents that its use would not infringe privately owned rights. Reference herein to any specific commercial product, process, or service by trade name, trademark, manufacturer, or otherwise, does not necessarily constitute or imply its endorsement, recommendation, or favoring by the United States Government or the University of California. The views and opinions of authors expressed herein do not necessarily state or reflect those of the United States Government or the University of California, and shall not be used for advertising or product endorsement purposes.

This is a preprint of a paper intended for publication in a journal or proceedings. Since changes may be made before publication, this preprint is made available with the understanding that it will not be cited or reproduced without the permission of the author.

Quantum-Based Atomistic Simulation of Materials Properties in Transition Metals

John A. Moriarty,* James F. Belak, Robert E. Rudd,

Per Söderlind, Frederick H. Streitz, and Lin H. Yang

Physics and Advanced Technologies Directorate

Lawrence Livermore National Laboratory

University of California

Livermore, CA 94551-0808 USA

(Dated: January 4, 2002)

Abstract

We present an overview of recent work on quantum-based atomistic simulation of materials properties in transition metals performed in the Metals and Alloys Group at Lawrence Livermore National Laboratory. Central to much of this effort has been the development, from fundamental quantum mechanics, of robust many-body interatomic potentials for bcc transition metals via model generalized pseudopotential theory (MGPT), providing close linkage between *ab initio* electronic-structure calculations and large-scale static and dynamic atomistic simulations. In the case of tantalum (Ta), accurate MGPT potentials have been so obtained that are applicable to structural, thermodynamic, defect, and mechanical properties over wide ranges of pressure and temperature. Successful applications discussed include structural phase stability, equation of state, melting, rapid resolidification, high-pressure elastic moduli, ideal shear strength, vacancy and self-interstitial formation and migration, grain-boundary atomic structure, and dislocation core structure and mobility. A number of the simulated properties allow detailed validation of the Ta potentials through comparisons with experiment and/or parallel electronic-structure calculations. Elastic and dislocation properties provide direct input into higher-length-scale multiscale simulations of plasticity and strength. Corresponding effort has also been initiated on the multiscale materials modeling of fracture and failure. Here large-scale atomistic simulations and novel real-time characterization techniques are being used to study void nucleation, growth, interaction, and coalescence in series-end fcc transition metals. We have so investigated the microscopic mechanisms of void nucleation in polycrystalline copper (Cu), and void growth in single-crystal and polycrystalline Cu, undergoing triaxial expansion at a large, constant strain rate – a process central to the initial phase of dynamic fracture. The influence of pre-existing microstructure on the void growth has been characterized both for nucleation and for growth, and these processes are found to be in agreement with the general features of void distributions observed in experiment. We have also examined some of the microscopic mechanisms of plasticity associated with void growth.

1. INTRODUCTION

Accurate and predictive large-scale atomistic simulation of materials properties is a forefront challenge in condensed-matter and materials physics. In principle, quantum mechanics can supply accurate total energies and interatomic forces for real materials, and to a large extent this has been realized in systems where electron-correlation effects are weak, including most bulk metals and semiconductors, through the use of *ab initio* electronic-structure methods based on density functional theory (DFT) [1, 2]. Even in the best of circumstances, however, the direct use of DFT methods to perform full quantum molecular-dynamics simulations [3, 4] on such systems is limited to a hundred or so atoms and a few picoseconds of simulation time. At the other extreme, classical molecular-dynamics (MD) simulations with short-ranged empirical potentials can now be done routinely for millions of atoms and nanoseconds of simulation time. Such simulations have been extremely useful in investigating generic phenomena in simple systems, but at the same time, they may not provide the desired physical accuracy for many real complex materials of interest. There is consequently a growing need to develop more accurate interatomic potentials, derived from quantum mechanics, that can be applied to large-scale atomistic simulations. This is especially so for directionally-bonded systems, such as transition and actinide metals, and for chemically or structurally complex systems, such as intermetallic compounds and alloys.

In metals, empirical radial-force potentials of either the embedded-atom (EAM) type [5] or the Finnis-Sinclair (FS) type [6] are the forms most often used in large-scale MD simulations. While these potentials are attractive for their computational efficiency and convenience, they are only physically well justified for simple *sp*-bonded metals and for series-end transition metals with filled or nearly filled *d*-electron bands, such as the noble metals. For central transition metals with partially-filled *d* bands, on the other hand, strong directional bonding is present that gives rise to non-radial forces and the need for explicit angular-force contributions to the interatomic potentials [7–9]. These contributions are found to be generally important to the structural and mechanical properties of such metals, so it is highly desirable to include them. In recent years, quantum-based interatomic potentials for transition metals that contain explicit angular-force contributions have been developed from tight-binding theory [9–11] and as well as from first-principles, DFT-based generalized pseudopotential theory (GPT) [7]. The latter include both *ab initio* GPT potentials [7, 12] and

simplified model-GPT or MGPT potentials [13, 14], which have been systematically derived from the first-principles theory. Many-body angular forces are accounted for in the MGPT through explicit analytic three- and four-ion potentials, and in this form the potentials are amenable to large-scale simulations in the central transition metals. Most recently, the MGPT potentials have been closely coupled to accurate *ab initio* DFT electronic-structure calculations on bcc metals such as tantalum (Ta) [15–18], providing a practical basis for the kind of robust and predictive simulation of materials properties that we seek.

In the present paper, we review recent and on-going research on quantum-based atomistic simulation of materials properties in transition metals carried out in the Metals and Alloys Group at Lawrence Livermore National Laboratory (LLNL). Our intent here is to provide a comprehensive overview of work on a wide range of structural, thermodynamic, defect and mechanical properties simulated at both ambient and extreme conditions of pressure, temperature, strain and strain rate. The primary focus will be on bcc metals and Ta in particular, where a unified description has been achieved via MGPT potentials, but we also discuss related work on void nucleation and growth in fcc copper (Cu) via EAM potentials, where new diagnostic tools are allowing us to do some pioneering real-time analysis of large-scale MD simulations. Our work on structural and thermodynamic properties is motivated by an interest in developing advanced multiphase equations of state, including an accurate treatment of high-pressure melting and liquid properties and the investigation of related phase transitions such as rapid resolidification on the short time scales (10^{-12} to 10^{-6} seconds) relevant to dynamic experiments. Our work on defects and mechanical properties, on the other hand, is motivated by a parallel interest in developing a predictive multiscale modeling capability to treat plasticity and strength, as well as fracture and failure. In this case, our atomistic simulations only represent the lowest length-scale component of a larger effort at LLNL and elsewhere to link simulations at multiple scales from atomistic to continuum and thereby provide a rigorous macroscopic description of mechanical behavior.

The remainder of this paper is organized as follows. In section 2, we discuss our computational approach, including the use of *ab initio* DFT electronic-structure calculations to constrain and validate MGPT potentials, together with our use of both standard and novel atomistic simulation techniques to apply the potentials. In section 3, we then consider the simulation of thermodynamic properties, including equation of state, melting, and rapid resolidification. The corresponding simulation of defects and strength properties is treated in

section 4, including elasticity and ideal shear strength, vacancies and self-interstitials, grain-boundary atomic structure, and the core structure and mobility of screw dislocations. In section 5, we present an overview of our related simulations on void nucleation and growth, and in section 6 we conclude by briefly discussing some current and future directions of our program.

2. COMPUTATIONAL APPROACH

The present quantum-based atomistic simulations are based on DFT quantum mechanics, as expressed in the well known local-density approximation (LDA) [2] to the treatment of exchange and correlation or in more recent extensions of the LDA such as the generalized-gradient approximation (GGA) [19]. The central focus of DFT methods is on obtaining the total energy of the electron-ion system, E_{tot} , as a functional of the electron density for a given configuration of the ions. For metals, two general strategies can be followed in this regard. The first and most widely used is to exploit the symmetry of the ion configuration and seek a direct numerical solution of the DFT equations. This leads to the usual *ab initio* electronic-structure techniques of condensed-matter theory. These techniques are chemically very robust, but are normally order- N^3 scaling with respect to the number of independent ion positions that can be treated. Thus they are practical only for relatively high-symmetry situations. An alternate and complementary strategy is to cast the electronic-structure problem into a form in which small quantities can be defined and used as a basis for rigorous expansions of the electron density and total energy. In real space, this leads to a multi-ion expansion of the total energy in terms of well defined *ab initio* interatomic potentials. Such techniques are order- N scaling and structurally very robust, but require truncation of the interatomic-potential series at low order, and possibly other simplifications, to be tractable for large-scale atomistic simulations. The close coupling of these two strategies is at the heart of present computational approach for transition metals, as we now describe.

2.1 *Ab initio* electronic-structure

A large number of reliable DFT electronic-structure techniques now exist, including both all-electron and pseudopotential methods. The role of these techniques in the present work

is two-fold. First, they provide accurate and fairly extensive data bases on fundamental, zero-temperature materials properties, which in turn can be used to constrain and validate MGPT potentials for transition metals over wide ranges of volume and pressure, as discussed below in section 2.2. Second, these methods can also be applied at finite temperature to provide additional electron-thermal contributions to calculated properties. This is explicitly needed, for example, to treat the equation of state, melting and other thermodynamic properties at high temperature, as further discussed in section 3.1 below. Here we first briefly summarize a few of the most important details of the specific *ab initio* electronic-structure methods used in our work, which include both full-potential linear muffin-tin orbital (FP-LMTO) and pseudopotential (PP) techniques. The all-electron FP-LMTO method can treat broad nearly-free-electron *sp* bands, narrower and more tightly-bound *d* bands, and very tightly-bound outer core states all on the same footing, so that the evolving electronic structure under pressure can be readily accomodated to arbitrarily high compression. In this regard, we have used the FP-LMTO method to study in detail basic structural, vibrational, elastic, and ideal-strength properties in Ta to 1000 GPa in pressure [15]. The *ab initio* PP approach has complementary strengths and in particular allows greater flexibility in treating relaxed defect structures. The FP-LMTO and PP methods have been used in tandem to study vacancy and self-interstitial formation and migration in Ta, as well as high-symmetry features of generalized stacking-fault (γ) energy surfaces [16, 17]. All of these results have been directly employed in the development and validation of our Ta MGPT potentials.

Our FP-LMTO and PP methods are fully implemented within first-principles DFT and use only the atomic number and the choice of either LDA or GGA exchange and correlation as input. In general, we have found that the GGA is the more accurate of the two approaches for bcc metals, especially for Ta, and our FP-LMTO calculations have used this treatment, except as noted. In both our FP-LMTO and PP approaches, the electron charge density and potential are allowed to have any geometrical shape and are calculated in a fully self-consistent manner. In our FP-LMTO method, all relativistic terms including spin-orbit can be included in the Hamiltonian for a heavy metal like Ta, while our PP method is inherently semi-relativistic. In addition, to represent the wave functions in Ta as accurately as possible in the FP-LMTO method, we have treated $5s$, $5p$, and $4f$ outer-core states on the same footing as the $6s$, $6p$, $5d$, and $5f$ valence states. With regard to defect calculations, we previously found that FP-LMTO-GGA and FP-LMTO-LDA vacancy formation energies

are the same in Ta, so all of the present point-defect calculations refer to the somewhat simpler semi-relativistic LDA treatment. All remaining FP-LMTO calculations have been done with the fully relativistic GGA treatment.

Extension of the FP-LMTO and PP methods to finite temperature is reasonably straightforward and effectively replaces the standard DFT formalism with the corresponding temperature-dependent Mermin formalism [20]. In practice, one introduces a Fermi-Dirac distribution function to populate the electron states at finite temperature, but retains the zero-temperature LDA or GGA forms for the exchange-correlation functionals. For a given configuration of ions, the self-consistent electronic-structure calculation then yields the electronic entropy and free energy in addition to the total energy. In the case of Ta, we have used finite-temperature FP-LMTO calculations to obtain the electron-thermal component of the multiphase equation of state and other thermodynamic properties over wide ranges of temperature and pressure [18]. In the high-temperature solid and in the liquid, this requires inputting snapshot ion configurations from MD simulations performed with corresponding MGPT potentials and then taking appropriate configuration averages, as further described in section 3.1.

2.2 Quantum-based interatomic potentials

Within the same DFT framework, generalized pseudopotential theory (GPT) provides a fundamental basis for *ab initio* interatomic potentials in elemental simple and transition metals [7]. In the GPT, a mixed basis set of plane waves and localized *d* states is used to expand the electron density and total energy of the metal in terms of weak *sp* pseudopotential, *sp-d* hybridization, and *d-d* tight-binding-like matrix elements. In a real-space formulation, the derived interatomic potentials become well-defined functionals of these matrix elements and all quantities can be evaluated directly from first-principles without any external input. For an elemental bulk metal, the GPT provides a rigorous expansion of the total energy in the form

$$\begin{aligned}
E_{\text{tot}}(\mathbf{R}_1 \dots \mathbf{R}_N) = & N E_{\text{vol}}(\Omega) + \frac{1}{2} \sum'_{i,j} v_2(ij; \Omega) + \frac{1}{6} \sum'_{i,j,k} v_3(ijk; \Omega) \\
& + \frac{1}{24} \sum'_{i,j,k,l} v_4(ijkl; \Omega) + \dots,
\end{aligned} \tag{1}$$

where $\mathbf{R}_1 \dots \mathbf{R}_N$ denotes the positions on the N ions in the metal, Ω is the atomic volume, and the prime on each sum over ion positions excludes all self-interaction terms where two indices are equal. The leading volume term in this expansion, E_{vol} , as well as the two-, three-, four- and higher multi-ion interatomic potentials, v_2, v_3, v_4, \dots , are volume dependent, but *structure independent* quantities and thus *transferable* to all bulk ion configurations, either ordered or disordered. This includes the liquid, as well as all structural phases of the solid. It also includes the deformed solid and the imperfect bulk solid with either point or extended defects present. The GPT formalism has also been extended to include surface environments [21] and to treat binary and ternary intermetallic compounds and alloys as well [12]. In addition, the GPT is systematically improvable in that the theory can provide any and all neglected higher-order terms in the electron-density and total-energy expansions. Currently, we explicitly treat *sp* interactions in total-energy terms up to and including v_2 and *sp-d* and *d-d* interactions in total-energy terms up to and including v_4 .

In practice, to perform both efficient and accurate atomistic simulations with GPT potentials, we normally terminate the total-energy expansion (1) at the lowest order that is consistent with the physics we seek to describe, and only introduce additional simplifications as required. For systems where directional bonding is unimportant, including, for example, most simple metals, series-end transition metals, and dilute transition-metal aluminides, only the volume and pair-potential terms need be retained. In such cases, full atomistic simulations can be carried out directly using the *ab initio* GPT potentials without further approximation [22]. For central transition metals, on the other hand, the angular-force, multi-ion potentials v_3 and v_4 reflect contributions from partially-filled *d* bands and are generally important to structural and mechanical properties. At the same time, however, in the full GPT these potentials are long-ranged, nonanalytic, and multidimensional functions, so that v_3 and v_4 cannot be readily tabulated for application purposes. This has led to the development of the model GPT or MGPT for bcc transition metals [13, 14]. Within the MGPT, the multi-ion potentials are systematically approximated by introducing canonical *d* bands and other simplifications to achieve short-ranged, analytic forms, which can then be applied to both static and dynamic simulations. To compensate for the approximations introduced into the MGPT, a limited amount of parameterization is allowed in which the volume-dependent coefficients of the modeled potential contributions are constrained by experimental or *ab initio* theoretical data. In this form, the MGPT indeed provides a robust

framework for performing accurate and predictive atomistic simulations on bulk transition metals.

Our original MGPT parameterization schemes for bcc metals, first developed for Mo [13, 14] and Nb [23], have recently been generalized and improved, including detailed application to the case of Ta [17]. In the improved scheme, the five volume-dependent d -state coefficients contained in v_2 , v_3 and v_4 , together with the volume term E_{vol} , are used to constrain the total energy and the multi-ion potentials. As a function of volume, these quantities are fit to theoretical and experimental data on the zero-temperature bcc equation of state, unrelaxed vacancy formation energy, shear elastic moduli, and Debye temperature, under the additional constraint of the so-called compressibility sum rule. The latter ensures that the bulk modulus calculated from volume derivatives of the total energy agrees with that calculated in the long-wavelength limit from position derivatives of the potentials. In the case of Ta, the constraining physical data have been obtained from our *ab initio* FP-LMTO results [15, 16], as slightly modified to maintain exact agreement with experiment near ambient conditions. We have so generated reliable Ta potentials over a wide volume range and extending up to 1000 GPa in pressure [17]. Many specific validation tests of the Ta potentials have been performed using additional experimental data as well as the results of our FP-LMTO and PP electronic-structure calculations. Several of these validating comparisons are presented below in sections 3 and 4.

2.3 Static and dynamic atomistic simulation

In the applications discussed in this paper, a number of different static and dynamic atomistic simulation methods have been employed, ranging from standard energy-minimization and molecular-dynamics techniques to new, specialized techniques, including a tailored MD approach to treat rapid resolidification [24] and a robust Green’s function method to treat dislocation core structure and mobility [17]. Except for the case of isolated dislocations, these approaches employ simulation supercells of adjustable size and fixed or variable shape to which periodic boundary conditions are applied. Additional external constraints may also be imposed, including conditions of constant volume, constant pressure or stress, constant strain or strain rate, and constant temperature. In most cases, the simulation codes used to implement these methods have been interfaced with both MGPT and EAM or FS potentials.

While MGPT potentials can provide the desired physical accuracy in bcc transition metals, they are necessarily more computationally intensive (currently by about a factor of 40) than short-ranged, radial-force EAM or FS potentials, so optimization of the simulation-cell size is highly desirable in large-scale applications. For the simulation of bulk thermodynamic properties, cells of a few hundred atoms are normally adequate and have been used in most of the present work, although a few simulations have been done with larger cells. In the future it will be interesting to consider much larger cells in the context of rapid resolidification. For the simulation of point and extended defects, simulation cells of a few thousand atoms are typically used to ensure adequate convergence, but this depends strongly on the particular application. Successful three-dimensional (3D) MGPT simulations of screw dislocations have used up to several hundred thousand atoms in static calculations on kink formation and very recently up to one million atoms in preliminary MD studies of dislocation motion. Our MD/EAM simulations of void nucleation and growth routinely use one to several million atoms.

Atomistic simulation of individual dislocations requires special treatment due to the long-ranged ($\sim 1/r$) elastic field associated with them. Historically, this elastic field has usually been treated with fixed boundary conditions [26, 27], but unless the simulation cell is very large, there will be a force build-up around the boundary between fixed and relaxed atomistic regions. To overcome such problems, Rao *et al.* [28] have developed efficient Green's-function-based flexible boundary conditions for both 2D and 3D dislocation simulations. In this technique, a buffer layer is introduced between the outer fixed and inner relaxed atomistic regions of the simulation cell, allowing one to dynamically update the boundary conditions of the simulation, while dramatically decreasing the size of the inner atomistic region. We have developed a fast and accurate parallel MGPT simulation code that combines Green's-function-based flexible boundary conditions with a spatial domain decomposition technique to calculate optimized dislocation structures in the presence of an arbitrary stress [17]. We have also recently developed a dynamic version of this code that will allow large-scale MD simulations of dislocation mobility and dislocation-defect interactions.

3. THERMODYNAMIC PROPERTIES

In this section we discuss the application of FP-LMTO electronic-structure and MGPT interatomic-potential methods to the calculation of thermodynamic properties of Ta over wide ranging conditions of pressure and temperature. In this regard, Ta is intended to serve as a prototype for the development of advanced capabilities to treat multiphase equations of state and phase transitions in complex metals. In treating such properties, it is useful to break all thermodynamic quantities into zero-temperature or cold, ion-thermal, and electron-thermal contributions, each of which may also be phase dependent as required. In the present case, one can conveniently write the total pressure, internal energy, and Helmholtz free energy of the metal for the phase α as

$$P^\alpha(\Omega, T) = P_0(\Omega) + P_{\text{ion}}^\alpha(\Omega, T) + P_{\text{el}}^\alpha(\Omega, T) , \quad (2)$$

$$E^\alpha(\Omega, T) = E_0(\Omega) + E_{\text{ion}}^\alpha(\Omega, T) + E_{\text{el}}^\alpha(\Omega, T) , \quad (3)$$

and

$$A^\alpha(\Omega, T) = E_0(\Omega) + A_{\text{ion}}^\alpha(\Omega, T) + A_{\text{el}}^\alpha(\Omega, T) , \quad (4)$$

respectively, at volume Ω and temperature T . Here the cold components P_0 and E_0 are intended to represent a single reference phase (bcc for Ta), and all phase dependence for additional solid phases and the liquid is absorbed into the ion- and electron-thermal components. The equation of state (EOS) of a material is represented by the functions $P^\alpha(\Omega, T)$ and $E^\alpha(\Omega, T)$, while $A^\alpha(\Omega, T)$ for the relevant phases α establishes the equilibrium phase boundaries between them. Below we present some of our preliminary results on the equation of state, melt, and rapid resolidification in Ta within this context. More complete accounts of this work will be published elsewhere [18, 25].

3.1 Multiphase equation of state

In considering the multiphase thermodynamic behavior of Ta, there are several specific phases of interest to consider. In the solid, the equilibrium bcc phase is predicted from *ab initio* FP-LMTO calculations [15] to be the stable ground state of this metal to at least 1000 GPa in pressure, as shown in figure 1. The high-pressure stability of the bcc phase has been confirmed in static diamond-anvil-cell experiments to 174 GPa at room temperature

[29] and is consistent with dynamic shock measurements [30, 31] up to and past the shock melting point near 300 GPa and 11,000 K. At the same time, it can be seen from the figure that the low-symmetry A15 structure is energetically competitive with bcc at low pressure and expanded volumes. While Ta is observed to melt out of the bcc structure, a metastable A15 phase has been reported during solidification of the undercooled liquid [32], and in our work, this latter phase is found to have interesting consequences for rapid resolidification more generally, as discussed in section 3.2 below. In particular, all of the qualitative structural features displayed in figure 1 are retained by the Ta MGPT potentials, allowing realistic simulation of the bcc-A15 competition. Thus the three specific phases of Ta we treat here are bcc, A15 and the liquid.

The cold bcc components P_0 and E_0 of our Ta EOS are taken directly from the *ab initio* FP-LMTO results in the 0-1000 GPa pressure range [15]. Since the cold EOS is an explicit constraint on our Ta MGPT potentials, these potentials exactly reproduce P_0 and E_0 . The potentials have then been used together with appropriate statistical methods to obtain the ion-thermal components P_{ion} , E_{ion} and A_{ion} for the phases of interest. In the low-temperature bcc solid, this is accomplished by means of standard quasi-harmonic lattice dynamics, which requires calculating detailed phonon spectra over an extended volume range. Towards this end, we have calculated phonons in bcc Ta as a function of volume over the range $1.26 \leq \Omega/\Omega_0 \leq 0.405$, where $\Omega_0 = 121.6$ a.u. is the observed equilibrium volume. Except for anomalous $T_2[110]$ modes at low pressure, the phonon frequencies are generally calculated to an accuracy of 10% or better, as benchmarked by experiment at ambient conditions and FP-LMTO results on high-symmetry zone-boundary phonons at high pressure. An important and revealing thermodynamic quantity is the ion-Grüneisen parameter, $\gamma_{\text{ion}} = \Omega dP_{\text{ion}}/dE_{\text{ion}}$, which is strongly volume dependent but nearly independent of temperature in the solid. Our calculated high-temperature quasi-harmonic result for γ_{ion} is displayed in figure 2. Near ambient conditions good agreement with experiment [33] is maintained, while at high compression a significant nonlinear volume dependence is predicted. The latter is in sharp contrast to the usual assumption that $\rho\gamma_{\text{ion}}$ is constant, where ρ is the density.

Ion-thermal energetics in the high-temperature solid and liquid, including both anharmonic effects in the bcc phase and investigation of the metastable A15 phase, have been obtained with MD simulations using our Ta MGPT potentials. Extensive simulations have been performed in a constant-volume, constant-temperature mode over the same extended

volume range indicated above and at temperatures up to the simulated melting point in the solid and up to 40,000 K in the liquid. These simulations have been done with a 250-atom computational cell for the bcc solid and the liquid and a 216-atom cell for the A15 solid. Typically, each simulation is started from a configuration at a nearby temperature, equilibrated for at least 50-60 picoseconds (ps) and then run an additional 30-40 ps to gather statistics. We thereby directly obtain $P_{\text{ion}}(\Omega, T)$ and $E_{\text{ion}}(\Omega, T)$ for the bcc solid and the liquid, while $A_{\text{ion}}(\Omega, T)$ is obtained through appropriate thermodynamic integration procedures [18]. Anharmonic effects are found to be small in bcc Ta, especially at low pressure. This is in sharp contrast to the case of Mo, where previous MD/MGPT simulations revealed large anharmonic effects [14]. The clear difference between Group-V metals (V, Nb, Ta) and Group-VI metals (Cr, Mo, W) in this regard has also been noticed previously in the analysis of experimental entropy data at ambient pressure [34].

The remaining electron-thermal components P_{el} , E_{el} and A_{el} are obtained by using finite-temperature FP-LMTO calculations and MD/MGPT simulations in tandem. For the low-temperature bcc solid, the FP-LMTO calculations can be done directly for the ideal bcc structure. For the high-temperature bcc solid and for the liquid, on the other hand, we have used snapshot MD configurations for small 27- or 54-atom cells as structural input into the FP-LMTO calculations and then configuration averaged to obtain thermodynamic properties. This procedure is computationally intensive but tractable and accurate. In particular, the small MD cells are adequate to approximate the structural details of the larger 250-atom cells, while only 10-15 configurations are needed to obtain converged thermodynamic averages. Figure 3 displays the electron-thermal component of the liquid entropy S_{el} so obtained for Ta. The results demonstrate a smooth and consistent behavior as a function of both volume and temperature. The quantitative magnitude of the calculated results also indicate the general importance of electron-thermal contributions to the thermodynamic properties of Ta at high temperature. In this regard, the electron-thermal component of the constant-volume specific heat closely approximates S_{el} and is in the range of 1-2 k_{B} near melt in liquid Ta.

Finally, the cold, ion-thermal and electron-thermal components for the bcc solid and the liquid have been assembled into full equations of state and free energies for each phase. The equilibrium melt curve has then been determined, as described below, and the bcc and liquid equations of state joined across this phase line. From these results it is possible to calculate

other thermodynamic properties of interest. Two important fundamental quantities are the room-temperature (300 K) isotherm and the principal shock Hugoniot. The former is obtained in the diamond-anvil-cell measurements, while the latter is the locus of final shock states obtained from successively stronger shocks imparted to the material initially at rest at ambient conditions. In figure 4 we compare our calculated 300 K isotherm and Hugoniot with experiment up to 300 GPa in pressure. The agreement between theory and experiment is generally good, with the calculated pressures above 100 GPa lying slightly higher than but within the error bars of the measured data.

3.2 Melting and rapid resolidification

The direct observation of melting in our MD/MGPT simulations provides only an upper bound to the equilibrium melt temperatures. This is because our 250-atom, constant-volume periodic simulation cell invariably leads to some superheating of the bcc solid. Likewise, the observed freezing transition provides only a lower bound to equilibrium melt due to corresponding undercooling of the liquid. This hysteresis is actually useful in practice, however, since it permits one to obtain ion-thermal energies, pressures and free energies above and below the equilibrium melt temperature at each volume considered for both the bcc and liquid phases. In addition, the electron-thermal free energy can then be directly added to the ion-thermal component for each phase in these regimes, allowing an accurate determination of the equilibrium Ta melt curve via the total bcc and liquid free energies. The result so obtained to 500 GPa in pressure is plotted in figure 5 together with the calculated temperature-pressure principal Hugoniot. As shown in the figure, the ambient-pressure melt temperature is in good agreement with experiment, as is the high initial melt slope, which has been measured in isobaric heating experiments [35]. In addition, the predicted crossing of the bcc Hugoniot with the melt curve is in good accord with the observed onset of shock melting near 300 GPa [31].

We find that the overall impact of the electron-thermal contributions to melting in Ta is to lower the calculated melt temperatures, but this effect is quantitatively much smaller than previously obtained in the case of Mo [14]. The reason for the difference between Ta and Mo is directly linked to the difference in the behavior of electronic density of states (DOS) at the Fermi level E_F as one crosses from the bcc solid into the liquid. In Mo the

bcc DOS at E_F is at a deep minimum and the corresponding liquid DOS is about a factor of two larger. In Ta, on the other hand, we find very little change in the DOS at E_F between the bcc solid and the liquid. At ambient pressure, these respective pictures of the electronic structure near melting in Mo and Ta are qualitatively confirmed by recent time-resolved photoelectron spectroscopy measurements [36].

In addition to melting, we have also explored the related issue of rapid resolidification from the liquid in Ta. Our initial MD/MGPT simulations in this regard were done in the same constant-volume and constant-temperature framework described above. A revealing quantity is the relative equilibrium ion-thermal energy, $E_{\text{ion}}^\alpha(\Omega, T)/3k_B T$, for the bcc, liquid and resolidified phases, as displayed in figure 6a at the measured equilibrium volume and in figure 6b for a highly compressed volume. These results demonstrate very clearly the contrasting behavior between resolidified Ta at low pressures, where there is strong competition between the bcc and A15 structures, and resolidified Ta at high pressures, where that competition is largely absent. At low pressures, freezing occurs into a complex glass structure of substantially higher energy than bcc, with $E_{\text{ion}}^{\text{glass}}$ almost independent of temperature. This glass structure has characteristics of both the bcc and A15 structures, as shown in figure 7 at 500 K. Specifically, the resolidified glass displays a radial pair correlation function $g(r)$ similar to that of the bcc structure, while an angular correlation function $b(\theta)$ similar to that of the A15 structure. In particular, the peak in $b(\theta)$ near 150° seen in both the glass and the A15 structure is a feature that is completely absent in the bcc structure. At high pressures, on the other hand, the resolidification transition in Ta results in direct recrystallization into the bcc structure, as shown in figure 6b. The recrystallized bcc phase is found to be structurally perfect without vacancies or other defects. This outcome is not a consequence, however, of the cubic cell shape, as the resolidified structure is randomly oriented with respect to the cell edges.

From this starting point, we have now embarked on a much more ambitious and comprehensive research program to address rapid resolidification in transition metals. As part of this effort, we have developed a more general MD simulation capability that allows precise, but minimally intrusive, temperature and pressure controls and real-time structural analysis on a variable-sized and -shaped simulation cell [24]. One can thereby model resolidification along any prescribed thermodynamic path for both central transition metals such as Ta (using MGPT potentials) and for simple or series-end transition metals such as Cu (using

EAM or GPT potentials). In the case of Ta, we have so investigated rapid resolidification from the liquid along paths of constant pressure (i.e., thermal quenches) and paths of constant temperature (i.e., rapid compressions) using 250-atom cells. The former confirm the above results of our initial simulations, with glass formation at low pressure and bcc recrystallization at high pressure. The latter isothermal compression paths also produce bcc recrystallization for final equilibrium pressure states above 100 GPa. Figure 8 illustrates four snapshots of a simulation initialized at 5000 K and ambient pressure and isothermally compressed to 300 GPa. During this simulation, the equilibrated liquid is rapidly compressed to near its final pressure in about 25 ps. The system then spends about 10 ps as an overpressurized liquid at 300 GPa before crystallizing into the bcc structure. More generally, the time spent by the system in such a metastable state is seen to depend sensitively on kinetic factors, including both the nature and energy separation of the competing solid phases and on the temperature and pressure of the final state relative to the melt curve. In preliminary simulations with cells containing thousands of atoms, regions of the metastable liquid are seen to partially order into the A15 structure, delaying the final crystallization into bcc by as much as several nanoseconds [25]. These simulations clearly demonstrate the close competition between A15 and bcc structures during rapid compression in Ta. We are also beginning to investigate Ta resolidification in much larger simulation cells to study carefully any additional size and environmental effects on these results.

4. DEFECTS AND MECHANICAL STRENGTH

In this section we turn our attention to the calculation of deformation and defect properties relevant to the mechanical strength of bcc metals. In this regard, the present Ta potentials have been rather extensively validated on a wide variety of such properties at both ambient pressure and high pressure, using available experimental data as well the results of *ab initio* electronic-structure calculations. Properties so considered here are high-pressure elastic moduli and the ideal shear strength, vacancy and self-interstitial formation and migration energies, and grain-boundary atomic structure. These results together with other validating calculations on γ surfaces [17] have in turn provided a sound basis for application of the Ta potentials to the core properties of $a/2 \langle 111 \rangle$ screw dislocations that control plasticity in bcc metals. We thus also discuss below recent results on the atomic

structure of the unstressed dislocation core, the formation of mobile kinks on the dislocation line at low stress, and the limiting Peierls stress required to move the rigid screw dislocation, together with the integration of these quantities into a useful model for dislocation mobility [17, 37, 38].

4.1 Elasticity and ideal shear strength

The single-crystal shear elastic moduli C_{44} and C' of the bcc solid are fundamental to its mechanical behavior and also serve as basic constraints on the MGPT potentials, as we have discussed above. At ambient pressure, values of the shear moduli and their first pressure derivatives are well established in Ta and other bcc metals through standard ultrasonic measurements [33]. At high pressure, on the other hand, we have relied on *ab initio* FP-LMTO calculations [15] to establish constraining values of C_{44} and C' to 1000 GPa. The resulting MGPT elastic moduli display rather smooth monotonic increases with pressure over this range, as shown in figure 9a. Interestingly, however, the corresponding anisotropy ratio, $A = C_{44}/C'$, is found to have more complex behavior as a function of pressure, as illustrated in figure 9b. At ambient pressure $A = 1.57$, but this ratio is predicted to rapidly decrease with pressure, reaching a minimum value of about 1.2 near 150 GPa. Beyond that point, A is seen to increase linearly with pressure, reaching a value of about 2.25 at 1000 GPa. The initial sharp decrease of A with pressure is consistent with the ultrasonic pressure derivatives of C_{44} and C' . This decrease has also been recently confirmed to about 100 GPa in Ta with a new stress and angle-resolved x-ray diffraction (SAX) method used in diamond-anvil-cell measurements [39]. The SAX technique has provided the first high-pressure measurements of elastic moduli in bcc metals. In figure 10 we compare our MGPT results with these data for C_{44} and C' individually. The agreement with experiment is especially good for C_{44} and is still quite reasonable for C' considering the large error bars in the SAX data. We are also developing a general method to treat the high-temperature thermoelastic properties of bcc metals by including additional ion-thermal and electron-thermal contributions to the elastic moduli.

A closely related fundamental mechanical property is the ideal shear strength of the perfect bcc crystal in the absence of dislocations or other defects. This quantity represents a theoretical upper limit to the actual yield stress for a given material. Following Paxton *et al.*

[40], we here identify the ideal shear strength with the maximum shear stress τ_c required for a continuous homogeneous deformation of the crystal into itself via the observed twinning mode. For bcc metals, this mode can be specified by a $[\bar{1}\bar{1}1]$ shear direction and a normal (112) slip plane. Apart from small tensile relaxations in this plane, the atomic positions during the deformation can be simply related to the relative amount of shear x/s along the twinning path. In particular, the unrelaxed calculation may be carried out entirely using a single atom per unit cell and periodic boundary conditions, allowing for direct application of the FP-LMTO electronic-structure method. In the case of Ta, self-consistent FP-LMTO calculations of the unrelaxed ideal shear strength have been performed at selected volumes in the 0-1000 GPa pressure range [15, 17] and may be compared with corresponding MGPT results. A representative comparison is shown in figure 11 at the observed equilibrium volume Ω_0 in terms of the energy barrier along the twinning path, $W(x) = (E_{\text{tot}}[x] - E_{\text{tot}}[0])/N$, and the associated stress along this path, $\tau(x) = (1/\Omega_0)dW(x)/dx$. The ideal shear strength τ_c is then identified with the maximum calculated stress along the twinning path. The good agreement displayed in figure 11 is maintained at high pressure as well, so the MGPT potentials can describe large shear deformations at both ambient and extreme conditions. In addition, the calculated unrelaxed shear strength under pressure displays a linear scaling with the shear modulus in the $\langle 111 \rangle$ direction, $G = (2C' + C_{44})/3$. For our MGPT results, we find that to a good approximation $\tau_c(P) = 0.12G(P)$ over the entire 0-1000 GPa pressure range.

4.2 Vacancies and self-interstitials

Point defects, including vacancies, self-interstitials and impurities, can have an important impact on the mechanical properties of metals. An important validation test of interatomic potentials in elemental bcc metals such as Ta is thus the calculation of fully relaxed vacancy and self-interstitial formation and migration energies. Here these defects are modeled within a large computational supercell containing N atoms in a volume Ω_N , with periodic boundary conditions applied in all three directions. At zero pressure, the formation energy for the defect is defined as $E^f = E_{\text{tot}}[N, \Omega_N] - NE_{\text{coh}}$, where E_{tot} is the relaxed total energy of the simulated system including the defect and E_{coh} is the cohesive energy per atom of the bulk solid at the equilibrium atomic volume Ω_0 . The corresponding formation volume is $\Omega^f =$

$\Omega_N - N\Omega_0$. Both volume and structural relaxation are normally included in the calculation, and the former necessitates that Ω_0 here be interpreted as the calculated zero-temperature equilibrium volume. For the self-interstitial formation energy, only the $\langle 110 \rangle$ split-dumbbell configuration has been considered, which previously has been shown to be the lowest-energy configuration for Mo [27]. The corresponding migration energy barriers are calculated by moving one atom, either the interstitial atom or a nearest-neighbor atom of the vacancy, from its equilibrium site towards a nearest-neighbor or vacancy site, respectively. During the migration process, the migrating atom is allowed to relax in the plane perpendicular to the migration path and all other atoms are fully relaxed subject only to the constraint that the simulation cell not rigidly shift. The migration energy is then $E^m = E^{\text{saddle}} - E^f$, where E^{saddle} is the formation energy of the defect at the saddle point. The assumed migration paths are taken along $\langle 111 \rangle$ for both the vacancy and self-interstitial, with the latter corresponding to the so-called jump and rotation path, previously calculated to be the one of lowest energy for Mo [27].

Table I summarizes calculated vacancy and self-interstitial formation and migration energies and formation volumes for Ta using the FP-LMTO, PP, and MGPT methods, together with available experimental data [41]. In the electronic-structure results, very efficient 36-, 48- or 54-atom supercells have been used. In the MGPT calculations, on the other hand, supercell size is not an important limitation, and much larger 250- and 1800-atom cells have been used for the vacancy and self-interstitial, respectively. In addition, a convenient alternative approach has been used in the MGPT migration-energy calculations that avoids the tedious volume relaxation [17]. Overall, there is good agreement between theory and experiment and between the electronic-structure results and the MGPT results. In particular, note that the characteristic low vacancy migration energy of group-V metals like Ta is well calculated by the MGPT potentials.

4.3 Grain-boundary atomic structure

Understanding the properties of grain boundaries and their interaction with dislocations and other lattice defects are matters of intrinsic importance to the multiscale modeling of strength and failure in polycrystalline materials. The prediction of grain-boundary atomic structure also represents an important validation test for interatomic potentials because

this is the one example of an extended defect where direct comparison with experiment is possible. In this subsection we briefly discuss recent MGPT simulations and experimental measurements on the $\Sigma 5$ (310)/[001] symmetric tilt boundary in prototype bcc transition metals, including Nb [42], Mo [43], and Ta [44]. This particular grain boundary is of special interest for several reasons. First, it has been possible to fabricate high-quality bi-crystals for this orientation and to study them experimentally with high resolution transmission electron microscopy (HREM). Second, it turns out that the distributions of bond lengths and bond angles at this boundary are similar to those occurring in the vicinity of a bulk screw dislocation, so important aspects of the MGPT potentials are indeed being tested. Finally, the actual atomic structure of the grain boundary is not a generic feature of bcc metals, but rather is material dependent and is a sensitive test of the angular forces [42, 45].

The first atomistic simulations on $\Sigma 5$ (310)/[001] grain boundary (GB) in Nb were performed with a Monte Carlo method [42], but subsequent studies performed at LLNL have used MD combined with a simulated annealing technique. The latter have successfully used both large simulation cells (up to 1960 atoms), with periodic boundary conditions in the GB plane and fixed boundary conditions along the [310] GB normal [43], as well as much smaller periodic cells [44, 45]. In a comprehensive study on Nb and Mo [45], MGPT results were also closely compared to parallel calculations with a DFT electronic-structure method, two separate tight-binding methods, tight-binding-based bond-order potentials [9], and FS potentials. To enable comparison with the DFT electronic-structure calculation, a minimal 20-atom periodic cell containing two GBs was used. Convergence was verified for all the potential methods using 40- and 80-atom cells. The 20-atom cell was then used to map out an energy surface along a prescribed path, beginning with the ideal coincident-site lattice configuration of the GB and ending with a full 3D relaxation of all the atoms. The resulting energy surfaces for Nb and Mo are given and discussed in reference [45] and for Ta in reference [44].

The two main structural issues for the $\Sigma 5$ (310)/[001] grain boundary are whether or not mirror symmetry is preserved across the boundary, and if not, what the magnitude of the relative atomic displacement along the [001] tilt axis is. Calculated MGPT and measured HREM results for Nb, Mo, and Ta are summarized and compared in Table II. In each case, the symmetry of the grain boundary has been correctly predicted by the MGPT potentials. In Mo and Ta, where the mirror symmetry is broken, the [001] atomic displacement is also

quantitatively consistent with experiment. The similarity between the atomic geometry of the $\Sigma 5$ (310)/[001] grain boundary and that of the $a/2$ $\langle 111 \rangle$ screw dislocation core is illustrated in figure 12, where the bond angles of near-neighbor atoms are plotted. In both the grain boundary and the dislocation, the distribution of angles is rather uniformly concentrated between about 50° and 150° , with very few high-angle configurations near 180° .

4.4 Dislocation core structure and mobility

The low-temperature and high-strain-rate plasticity of bcc metals is controlled by the intrinsic core properties of $a/2$ $\langle 111 \rangle$ screw dislocations. Unlike the highly mobile edge dislocations in these metals, the motion of the screw dislocations is severely restricted by the nonplanar atomic structure of its core, resulting in low mobility, thermal-activated kink mechanisms, and a temperature-dependent yield stress. In this final subsection we discuss our atomistic simulations on individual $a/2$ $\langle 111 \rangle$ screw dislocations in bcc Ta using MGPT potentials and Green’s-function flexible-boundary-condition (GFBC) methodology.

4.4.1 Ground-state core structure. The stable ground-state core configuration of the $a/2$ $\langle 111 \rangle$ screw dislocation is centered among three $\langle 111 \rangle$ atomic rows forming a triangular prism. Around these three rows the near-neighbor atoms are positioned on a helix that winds up in a clockwise or counter-clockwise manner (see figure 13), depending on the location of the elastic center and the sign of the Burgers vector \mathbf{b} . In general, the ground-state core exhibits three-fold directional spreading along three $\langle 112 \rangle$ directions on $\{110\}$ planes. This can happen in two distinct but energetically equivalent ways, resulting in a doubly degenerate core. Under the right circumstances, however, the spreading may vanish, resulting in an isotropic and nondegenerate core with a higher six-fold symmetry. In the present work, the atomic core structure in bcc Ta has been simulated using a 2D GFBC technique in cylindrical geometry, with periodic boundary conditions along the $\langle 111 \rangle$ direction. Near ambient pressure conditions we predict a nearly isotropic but still three-fold symmetric and doubly degenerate core, whose detailed structure is most easily displayed using the standard differential displacement method [26]. In this method, the $\langle 111 \rangle$ screw components of the relative displacement of neighboring atoms due to the dislocation is represented by an arrow between the two atoms. The calculated screw-component map for Ta is shown in figure 14a.

A corresponding map can also be constructed for the perpendicular edge components of the dislocation as well. For the edge displacements, which are much smaller in magnitude, the direction of the arrow indicates the direction of the relative displacement component normal to the $\langle 111 \rangle$ direction. The calculated edge-component map is displayed in figure 14b.

Our calculated core structure for Ta may also be compared to other recent calculations by different methods. Duesbery and Vitek [46] obtained an isotropic, six-fold symmetric core using FS potentials in a fixed-boundary-condition atomistic simulation. An isotropic core structure for Ta was also obtained by Ismail-Beigi and Arias [47] in the first *ab initio* PP dislocation calculation. In the latter approach, a quadrupolar arrangement of four dislocation cores in a small computational cell containing only 90 atoms with periodic boundary conditions was considered. Most recently, Woodward and Rao [48] have performed an *ab initio* PP calculation of the Ta core using an adaptation of the GFBC method to DFT electronic-structure calculations. They too obtain an isotropic core structure. It is thus interesting and noteworthy that all four studies, by four very distinct methods, conclude that the equilibrium Ta core structure is either isotropic or very nearly so.

Our studies of the Ta core structure have been extended to high pressure as well [38] and reveal the additional interesting result that the precise core structure depends sensitively on the volume or pressure conditions considered. This effect is most readily quantified by the so-called polarization \mathbf{p} of the degenerate core. This polarization measures the simultaneous translation of the three central atoms nearest to the core center. This translation is parallel to the dislocation line but in opposite sense for the two different core orientations (commonly denoted as positive p and negative n). When \mathbf{p} vanishes, the two core configurations coincide and a fully symmetric or isotropic core structure with a higher six-fold symmetry is obtained. At $\mathbf{p} = \pm \mathbf{b}/6$, on the other hand, a fully polarized core is obtained with maximum three-fold spread out along $\langle 112 \rangle$ directions. While our calculated magnitude of the polarization of the equilibrium core is indeed very small, $0.004(b/6)$, we find that the core polarization is a rapidly increasing function of pressure, as illustrated in figure 15 up to 20 GPa. At higher pressure, this effect is even more dramatic and large polarizations can occur [38]. Conversely, under modest expansion (i.e., negative pressure), the polarization will indeed exactly vanish. Thus in general, one can expect a continuum of $a/2 \langle 111 \rangle$ screw dislocation core structures between the isotropic and fully polarized limits.

4.4.2 Kink-pair formation. At finite temperature, the motion of the screw dislocations in the bcc lattice normally occurs by the thermally assisted formation and migration of kink pairs. For low-stress conditions, the individual kinks in a kink pair are well separated and weakly interacting, so kink-pair formation can be studied by just looking at isolated kink formation. In this limit, the nature and atomic structure of the possible kinks is closely related to the unstressed dislocation core. The doubly-degenerate core structure results in different possible kinks and kink-pair configurations involving p and n segments that can be formed. In addition, p and n segments can co-exist on the same dislocation line in the form of a so-called anti-phase defect (APD). In general, two different anti-phase defects on the dislocation line (np and pn) and six distinct and nondegenerate kinks are geometrically possible [49]. To accurately model an isolated kink, a 3D simulation cell is used in the form of a long compliant cylinder centered on the dislocation line but locally adapted to the kink geometry. We consider here only kinks formed on $\{110\}$ planes. Kinks formed on other planes such as $\{211\}$ have significantly larger kink heights and therefore are either unstable or have much larger kink formation energies [27]. The atomic structures and formation energies of the remaining possible APDs, isolated kinks, and kink pairs in Ta have been calculated and elaborated in detail [17]. The core structure of the lowest-energy isolated left kink is illustrated in figure 16. The corresponding lowest energy kink pair that can be formed from isolated left and right kinks without a pre-existing APD has a formation energy of 0.96 eV. This value is in close agreement with the empirical zero-stress activation enthalpy of 1.02 eV currently used in microscale dislocation-dynamics simulations to model the temperature-dependent yield stress and plastic flow in bcc Ta [50]. For this kink pair we have also investigated the related issue of kink migration, which is limited by the secondary Peierls stresses needed to move the left- and right-hand kinks. We calculate these secondary stresses to be 1-2 orders of magnitude smaller than the corresponding Peierls stress τ_P for the rigid screw dislocation itself (see below), so both kinks are expected to be mobile. Consequently, the dislocation velocity at low stress should be controlled by kink-pair formation rather than kink migration.

At smaller finite separation, the left and right kinks will elastically attract each other, requiring an applied shear stress to maintain the separation. During the kink-pair activation process, the energy required to generate the kink pair is supplied partly by thermal activation and partly by the work done by the applied shear stress needed to maintain the pair at

separation distance λ . The stress-dependent activation enthalpy for the balanced kink pair is given by

$$\Delta H(\tau) = E_{\text{tot}}^{\text{f}}(\tau) - \tau \lambda(\tau) h b , \quad (5)$$

where $E_{\text{tot}}^{\text{f}}$ is the total formation energy of the kink pair under the applied stress τ . In the microscale dislocation-dynamics (DD) simulations, it is assumed that the screw dislocation velocity is directly proportional to $\exp[-\Delta H(\tau)/k_{\text{B}}T]$, so ΔH is a key input parameter for the DD simulations. At small levels of stress, $\tau < 0.2\tau_{\text{P}}$, the activation enthalpy ΔH can be obtained directly from stress-separation (τ - λ) and energy-separation ($E_{\text{tot}}^{\text{f}}$ - λ) MGPT/GFBC atomistic simulation data on interacting but still well separated kinks [17]. At higher levels of stress, $\tau > 0.2\tau_{\text{P}}$, however, special methods must be applied which allow the dislocation line itself to move and begin to climb the Peierls barrier in a self-consistent manner [37]. We have thereby obtained ΔH in bcc Ta to above $0.6\tau_{\text{P}}$ and fitted the atomistic data to an analytic form currently used in DD simulations as a function of τ/τ_{P} . These results are displayed in figure 17 and compared with the empirical DD result based on the observed yield stress in Ta. The agreement is clearly very good.

4.4.3 Peierls stress. To complete this double-kink mobility model, one must address the high stress limit and consider the magnitude and orientation dependence of the Peierls stress to move the straight screw dislocation. In bcc metals, slip predominantly takes place in $\{110\}$ and/or $\{112\}$ planes at low temperatures. In a bcc crystal along a given $\langle 111 \rangle$ direction, there are three $\{110\}$ planes and three $\{112\}$ planes, mutually intersecting every 30° . Because of the twinning–anti-twinning asymmetry in the bcc lattice, unique values of the critical resolved shear stress (CRSS) can exist on different planes ranging in orientation from $\chi = -30^\circ$ (twinning orientation on $\{211\}$) to $\chi = 30^\circ$ (anti-twinning orientation on $\{211\}$), with χ being the angle measured from a given $\{110\}$ slip plane. We have studied this stress-orientation geometry in bcc Ta for pure shear and selected uniaxial loadings [17]. The calculated results for pure shear loading are displayed in figure 18. As shown in the figure, the CRSS is found to depend strongly on the orientation of the loading axis, remaining almost constant from $\chi = -30^\circ$ to $\chi = 0^\circ$, but then rising rapidly between 0° and 30° . Our minimum calculated Peierls stress τ_{P} occurs for a pure shear stress with $\chi = -10^\circ$ and has a magnitude of $9.4 \times 10^{-3}G = 590$ MPa. This value is about a factor of four smaller than calculated with simple FS potentials and fixed boundary conditions

for Ta at the same stress orientation [51]. At the same time, our value is still about a factor of two larger than the best available empirical estimate under similar, although not identical, stress-orientation conditions [50, 52]. The reasons for this latter disagreement are not clear at present, but there are several possibilities. On the experimental side, there is no actual direct measurement of the Peierls stress for an isolated dislocation, but only an inferred value obtained by extrapolating the temperature dependence of the yield stress for a deformed single crystal to zero temperature. On the theoretical side, the disagreement could reflect a limitation in either the present Ta MGPT potentials or in the method of simulation. With regard to the latter, our 2D zero-temperature calculation may possibly miss very low energy 3D and/or dynamic kink-like processes that would lead to an effectively lower Peierls stress. Such a mechanism has been argued to be operative in the case of edge dislocations for bcc metals [53]. We are currently performing 3D finite-temperature MD simulations to investigate this possibility.

5. VOID GROWTH AND DYNAMIC FRACTURE

In this section we examine how atomistic simulation is being used to investigate the microscopic origins of dynamic fracture in metals. When an explosive is detonated near a metal surface or tensile shock waves overlap inside a ductile metal, extreme states of tension are created and internal failure occurs through the nucleation, growth, and linking of microscopic voids [54]. The resulting dynamic fracture inside a metal plate can cause a scab to form and fly off of the back surface. This process, known as spallation, has been the subject of extensive metallurgical investigation [55–57]. While there have been many continuum level studies of void growth in this context [58–61], very little is known about the microscopic mechanisms by which voids nucleate and grow.

5.1 Atomistic simulation of dynamic-fracture processes

In order to examine the microscopic processes of dynamic fracture in detail, we have developed a direct numerical simulation of void nucleation and growth using large-scale molecular dynamics [62, 63]. The initial focus has been on fcc metals, where the noble metal Cu has served as a prototype system and has been extensively studied using a reliable EAM

potential due to Oh and Johnson [64]. High-strain-rate isotropic (triaxial) tensile loading is applied by expanding a cubic simulation box at a constant rate. Strain rates of 10^9 through 10^{11} s^{-1} have been considered, and periodic boundary conditions are used to simulate a region inside a bulk metal. In our first Cu simulations [62, 63], we studied homogeneous void nucleation in a single crystal and void nucleation at grain boundaries and grain-boundary junctions. The model was later extended to the growth of an isolated void [65, 66], and recently important new on-the-fly methods of characterization have been developed that are providing major insight into all the void simulations [67]. In each case, an initial configuration of the system is constructed, brought to equilibrium at room temperature under fixed volume conditions, and then allowed to expand at a constant strain rate with the thermostat turned off. The simulation cell sizes have varied, but typically a million or a few million atoms in a periodic box is simulated. Further details are discussed in references [63, 66, 67].

In order to validate the modeling and focus it on the relevant physical phenomena, a concurrent experimental program has also begun at LLNL [68]. This program involves systematically shocking and recovering metals with known initial microstructure (including single-crystal and polycrystal Cu and Al and single crystal Cu with internally oxidized silica inclusions). By varying the stress and pulse duration, a state of incipient damage is created. The samples are studied using 2D optical and electron microscopy and 3D X-Ray tomography. The 2D electron microscopy reveals information about the dislocation structure surrounding an arrested void. The 3D X-Ray tomography reveals the full 3D distribution of voids and the manner by which they link to form the fracture surface. Concurrently, the free-surface velocity is measured to infer the stress transient. The difference in the shock velocity and the velocity when the material fails is related to the stress at which fracture occurs, also known as spall strength [69].

5.2 Plasticity associated with voids

Void growth induces plastic deformation of the surrounding material in order to accommodate the increase in the volume of the void as it grows. Initially pre-existing voids stretch elastically when a tensile stress is applied, but eventually the deformation becomes large enough that the surface is unstable to the emission of dislocations. The growth of the void and the concomitant plasticity are interrelated, and it is important to understand the evo-

lution of the plastic field around the void in order to understand the growth of the void and the initial phase of fracture. The slip associated with dislocations allows material to be transported away from the void in order to enlarge the cavitated region, and the ease with which this slip takes place depends on the state of plasticity. Dislocations that lie in the neighborhood of the void can interact with dislocations emitted as the void grows. For example, dislocations emanating from the void can collide with forest dislocations on other glide systems forming sessile junctions. Whether the forest dislocations are present or not has a significant impact on the evolution of the plastic field around the void, and this in turn affects the rate of void growth. An important goal of the void simulations is to understand this connection in detail.

5.2.1 Structural characterization. It is crucial to these simulations to be able to compute the evolving dislocation structure on the fly. The simulations we discuss here contain a million or more atoms, and to store all of the data for these atoms at each time step would be prohibitive both in terms of overall storage requirements and in terms of I/O time. We have developed a set of dislocation analysis tools that allow the dislocation structure to be analyzed on the fly at a negligible computational expense. The tools are based on a set of local structural characteristic functions defined for each atom in the simulation that can distinguish between different atomic environments at finite temperature. The technical details will be described elsewhere [67], but the basic idea is straightforward. The method is a generalization of previous techniques used to identify atoms that participate in dislocation cores based on their energy [70, 71]. In the latter, potential energy is used to discriminate between atoms at defects and those at non-defective, albeit somewhat deformed, crystalline sites, noting that the atoms at defects such as dislocation cores, vacancies and surfaces have a higher potential energy. The energy discrimination technique was designed for zero temperature, however. At room temperature in Cu, thermal fluctuations are comparable in magnitude to the dislocation core energies, so energy discrimination can not be used directly. We have tried to quench an atomic configuration to zero temperature but have found the dislocation structure to change in subtle ways. For example, the stair-rod connecting the different segments of a prismatic loop relax towards their equilibrium size. The structural characterization we have developed is based on generalizations of the centrosymmetry deviation [72] and other symmetry-deviation parameters that have been adapted for finite

temperature. Figure 19 shows two snapshots of the same dislocations emerging from a growing void in Cu at room temperature, dramatically contrasting identification by energy characterization and by symmetry-deviation-based structural characterization.

The computation of the symmetry deviation parameters is fast and parallelizable. It adds a few percent to the total execution time for our MD simulations. Figure 20 shows a typical result. Of the entire simulation, only those atoms with a symmetry deviation parameter greater than a threshold are plotted. The threshold is set by the tail of the peak in the symmetry deviation distribution associated with the bulk (non-defective) atoms. This is important since the actual values of each defect evolve with the macroscopic state of the simulation: the temperature, the mean stress, etc. Once the location of the dislocations is identified, the full Burgers vector information is generated automatically by comparison with a reference configuration.

5.2.2 Void nucleation. We have simulated the homogeneous nucleation of voids in single-crystal Cu and the heterogeneous nucleation of voids in polycrystalline Cu [62, 63, 66]. In single-crystal Cu, the calculated spall strength at room temperature (9 GPa) is much greater than the observed spall strength in macroscopic samples (1.5-4.5 GPa [73]). The mean spacing between nucleated voids in this case is found to vary inversely with strain-rate with slower rates allowing more time for the material surrounding a void to release elastically.

Polycrystalline Cu has been simulated by choosing four seed sites, either at random positions or on a close-packed lattice, and filling space with a randomly oriented grain out to the Voronoi boundary with the neighboring grains. The system was annealed at 900 K to allow the grain boundaries to relax and returned to room temperature before the tensile strain was applied. Voids typically nucleate at weak points in the material, and grain boundary junctions offer one such preferred nucleation site. It has been observed in many experiments that in the initial phase of dynamic fracture, the nucleation and growth of voids is highly correlated with pre-existing grain boundaries [73]. This is what is observed in our simulations of polycrystalline Cu subjected to a constant hydrostatic strain rate [62, 63, 66]. The voids nucleate at the grain boundary junctions, and then void growth occurs along the grains until the point where the voids get close enough to begin necking out toward each other in preparation for coalescence.

There is a broad array of dislocation activity that is observed in these simulations [66]. The primary growth mechanism involves the growing voids punching out dislocations in a mechanism that transports platelets of interstitial atoms away from the void, allowing it to grow. In the case of growth of voids in single-crystal material, these platelets are interstitial prismatic loops, but in the case of a void at a grain boundary, the loops typically terminate on the grain boundary and are not full prismatic loops. Some full prismatic loops have been observed, but they account for very little of the total dislocation activity. The grain boundaries are also very active in the simulated evolution of the plastic zone [66]. They absorb and emit dislocations actively.

5.2.3 Void growth. We have also simulated the growth of a pre-existing void in a single crystal of an fcc metal [65, 67]. The initial state of the simulation is a single crystal of Cu with a 2 nm radius spherical void cut from the center of the computational cell. This simulation is very useful in two aspects. Firstly, it gives insight into the growth of a void in a relatively simple, uncluttered system where the analysis is straightforward, and it is easier to make contact with continuum models. Secondly, it is directly relevant to the growth of voids that are nucleated at weakly bound inclusions, such as the planned LLNL incipient spallation experiments using Cu with internally oxidized silica inclusions.

These void-growth simulations have shown dislocation activity that is classic in many regards, but they have also offered some surprises at the nanoscale. The primary mechanism of the evolution of the plastic zone, at least on the time scales accessed by the MD simulations, is the punching out of interstitial prismatic loops in order to allow the void to grow. The loops are evident in figure 20. This mechanism is familiar from other situations in which a spherical interface expands without diffusion across it: the thermal expansion of inclusions and the growth of helium bubbles.

Once these loops are emitted from the surface of the void, they begin to glide away. In some cases this motion is unimpeded by other dislocations, and the velocity of the loops can reach a significant fraction of the shear wave speed in the material despite finite temperature phonon drag. In other cases, the prismatic loop may not propagate ballistically due to a collision with another dislocation near the surface of the void. If they form a sessile junction, the loop becomes trapped at the void surface. This leads to the formation of a skin of highly defective material about the void, and the complete emission of the loop is substantially

delayed, in many cases past the end of the simulation. Subsequent loop emission then comes from this highly defective region and not from a pristine void surface. Thus, the evolution of the plastic zone depends on whether forest dislocations are present, and this depends on the shape of the void. The details will be presented elsewhere [67], but this indicates the intimate interplay between the void growth and the concomitant plasticity.

5.3 Beyond atomistic simulation

Even though the void simulations contain a million or more atoms, the size of the system is small and the time scale is short compared to all but the strongest laser shock experiments. We need to go to larger system sizes and longer time scales in order to compare directly with the on-going LLNL experiments. Also, larger system sizes are necessary to make contact with microscale and mesoscale simulations such as dislocation dynamics [74] and continuum simulations such as cohesive zone modeling [75]. In principle, our atomistic simulations can supply needed input into the latter approaches, but actually bridging the length-scale gaps remains a major multiscale modeling challenge.

One way we are addressing the need for larger systems is to use so-called concurrent multiscale modeling. The idea of concurrent multiscale modeling is to hybridize MD with a more coarse-grained model such as the finite element method (FEM). The MD is used in the fully resolved central region (such as near a void), while FEM is used to capture the long-range strain fields that extend into the periphery. The MD and the FEM are run concurrently within the same simulation, each one in essence providing the correct dynamic boundary conditions for the other. This formalism was developed previously for semiconductors [76–78] and it has recently been extended to metals [79]. The ultimate goal is to allow dislocations to propagate into the coarse-grained region, but this is still an open problem for 3D dynamic simulation.

6. CURRENT AND FUTURE DIRECTIONS

In the present paper we have summarized recent progress in developing advanced quantum-based atomistic simulations of materials properties in transition metals. For directional-bonded bcc transition metals such as Ta, the combination of fundamental DFT-

based generalized pseudopotential theory and accurate *ab initio* electronic-structure calculations have produced robust MGPT interatomic potentials applicable to large-scale atomistic simulations of a wide range of thermodynamic and mechanical properties at both ambient and extreme conditions. This is enabling the development of advanced multiphase equations of state and the treatment of phase transitions, including those associated with complex kinetic phenomena such as occur in rapid resolidification. At the same time, the accurate atomistic simulation of point defects, grain boundaries and dislocations, together with the development of new simulation and diagnostic capabilities for treating the nucleation and growth of voids, is establishing a sound foundation for the predictive multiscale modeling of strength and failure. In particular, the stage has been set for the direct linkage of atomistic and higher-length-scale simulations, including microscale dislocation dynamics and the continuum finite element method.

Many specific challenges await, and we mention only a few current and future research directions. In the area of rapid resolidification, we are developing a massively parallel MD/MGPT simulation code specialized to this application that will allow us to treat very large systems and to investigate the environmental, size, and temporal factors controlling the morphology of the resolidified solid. In the area of dislocation mobility, our calculated kink and kink-pair energetics for Ta appear to be consistent with current microscale dislocation-dynamics simulations of single-crystal plasticity. At the same time, in the high-stress limit there is still an apparent factor of two disagreement with experiment regarding the magnitude of the Peierls stress that needs to be resolved to develop a fully quantitative mobility model. We are extending the 2D Peierls-stress calculations discussed here to dynamic 3D simulations at finite temperature to further investigate this issue and also to study double-kink formation at high stress. In the area of void nucleation and growth, extension of our current MD/EAM simulations on fcc metals to bcc transition metals described by MGPT potentials should be possible and is planned for the near future. Regarding the MGPT potentials themselves, various extensions and systematic improvements are also planned, including the treatment of f-electron actinide metals, the direct incorporation of electron-thermal effects to produce temperature-dependent potentials, and the development of optimized matrix representations to increase computational speed and permit the treatment of higher-order interactions.

ACKNOWLEDGMENTS

This work was performed under the auspices of the U.S. Department of Energy by the University of California Lawrence Livermore National Laboratory under contract number W-7405-ENG-48.

* E-mail: moriarty2@llnl.gov

- [1] Hohenberg P and Kohn W 1964 *Phys. Rev.* **136** B864
- [2] Kohn W and Sham L 1965 *Phys. Rev.* **140** A1133
- [3] Car R and Parrinello M 1985 *Phys. Rev. Lett.* **55** 2471
- [4] Kresse G and Hafner J 1993 *Phys. Rev. B* **47** 558
- [5] Daw M and Baskes M 1983 *Phys. Rev. Lett.* **50** 1285
Daw M and Baskes M 1984 *Phys. Rev. B* **29** 6443
Daw M, Foiles S M and Baskes M 1993 *Mater. Sci. Rep.* **9** 251
- [6] Finnis M and Sinclair J 1984 *Phil. Mag. A* **50** 45
Ackland G J and Thetford R *Phil. Mag. A* **56** 15
Ackland G J and Vitek V 1990 *Phys. Rev. B* **41** 10324
- [7] Moriarty J A 1988 *Phys. Rev. B* **38** 3199
- [8] Carlsson A 1990 *Solid State Physics: Advances in Research and Applications* vol 43 (Boston: Academic Press) p. 1
- [9] Pettifor D G 1989 *Phys. Rev. Lett.* **63** 2480
Pettifor D G, Aoki M, Gumbsch P, Horsfield A P, Nguyen-Manh D and Vitek V 1995 *Mater. Sci. Eng. A* **192/193** 24
- [10] Carlsson A 1991 *Phys. Rev. B* **44** 6590
- [11] Foiles S M 1993 *Phys. Rev. B* **48** 4287
- [12] Moriarty J A and Widom M 1997 *Phys. Rev. B* **56** 7905
Widom M and Moriarty J A 1998 *Phys. Rev. B* **58** 8967
Widom M, Al-Lehyani and Moriarty J A 2000 *Phys. Rev. B* **62** 3648
- [13] Moriarty J A 1990 *Phys. Rev. B* **42** 1609
- [14] Moriarty, J A 1994 *Phys. Rev. B* **49** 12431
- [15] Söderlind P and Moriarty J A 1998 *Phys. Rev. B* **57** 10340
- [16] Söderlind P, Yang L H, Moriarty J A and Wills J M 2000 *Phys. Rev. B* **61** 2579
- [17] Yang L H, Söderlind P, and Moriarty J A 2001 *Phil. Mag. A* **81** 1355
- [18] Moriarty, J A and Söderlind P 2002 *Phys. Rev. B* to be published
- [19] Perdew J, Chevary J, Vosko S, Jackson K, Pederson M, and Singh D 1992 *Phys. Rev. B* **46**

- [20] Mermin N D 1965 *Phys. Rev.* **137** A1441
- [21] Moriarty J A and Phillips R 1991 *Phys. Rev. Lett.* **66** 3036
- [22] Moriarty J A and Althoff J D 1995 *Phys. Rev. B* **51** 5609
Greef C W and Moriarty J A 1999 *Phys. Rev. B* **59** 3427
- [23] Moriarty, J A 1990 in *Many-Atom Interactions in Solids* (Berlin: Springer) p. 158
- [24] Streitz F H 2002 *J. Chem. Phys.* to be published
- [25] Streitz F H and Moriarty J A 2002 *Phys. Rev. Lett.* in preparation
- [26] Vitek V 1974 *Cryst. Lattice Defects* **5** 1
- [27] Xu W and Moriarty J A 1996 *Phys. Rev. B* **54** 6941
Xu W and Moriarty J A 1998 *Comput. Mater. Sci.* **9** 348
- [28] Rao S, Hernandez C, Simmons J, Parthasarathy T and Woodward C 1998 *Phil. Mag. A* **77** 231
- [29] Cynn H and Yoo C-S 1999 *Phys. Rev. B* **59** 8526
- [30] Mitchell A C and Nellis W J 1981 *J. Appl. Phys.* **52** 3363
- [31] Brown J M and Shaner J W 1984 *Shock Waves in Condensed Matter - 1983*, ed Asay J R, Graham R A and Straub G K (Amsterdam: Elsevier) p. 91
- [32] Cortella L, Vinet B, Desré P J, Pasturel A, Paxton A T and van Schilfgaarde M 1993 *Phys. Rev. Lett.* **70** 1469
- [33] Katahara K W, Manghnani M H and Fisher E S 1979 *J. Phys. F: Metal Phys.* **9** 773
- [34] Eriksson O, Wills J M and Wallace D 1992 *Phys. Rev. B* **46** 5221
- [35] Shaner, J W, Gathers, G R and Minichino C 1977 *High Temp.-High Pres.* **9** 331
- [36] Oelhafen P, Wahrenberg R and Stupp H 2000 *J. Phys.: Condens. Matter* **12** A9
- [37] Yang L H, Tang M and Moriarty J A 2001 *Multiscale Modeling of Materials-2000* MRS Symp. Proc. vol 653, ed Kubin L P, Bassani J L, Cho K, Gao H and Selinger R L B (Warrendale, PA: Materials Research Society) p. Z1.2.1
- [38] Yang L H, Söderlind P and Moriarty J A 2002 *Phys. Rev. Lett.* in preparation
- [39] Cynn H and Yoo C-S 2002 *Phys. Rev. B* to be published
- [40] Paxton A T, Gumbsch P and Methfessel M 1991 *Phil. Mag. Lett.* **63** 267
- [41] Schultz H and Ehrhart P 1991 *Atomic Defects in Metals, New Series, Group III* (Springer: Berlin)

- [42] Campbell G H, Foiles S M, Gumbsch P, Rühle M and King W E 1993 *Phys. Rev. Lett.* **70** 449
- [43] Campbell G H, Belak J and Moriarty J A 1999 *Acta Mater.* **47** 3977
- [44] Campbell G H, Belak J and Moriarty J A 2000 *Scripta Mater.* **43** 659
- [45] Ochs T, Elsässer C, Mrovec M, Vitek V, Belak J and Moriarty J A 2000 *Phil. Mag. A* **80** 2405
- [46] Duesbery M S and Vitek V 1998 *Acta mater.* **46** 1481
- [47] Ismail-Beigi S and Arias T A 2000 *Phys. Rev. Lett.* **84** 1499
- [48] Woodward C and Rao S I 2001 *Phil. Mag. A* **81** 1305
- [49] Duesbery M S 1983 *Acta metall.* **31** 1747
- [50] Tang M, Kubin L P and Canova G R 1998 *Acta Mater.* **46** 3221
Tang M 2000 private communication
- [51] Ito K and Vitek V 2001 *Phil. Mag. A* **81** 1387
- [52] Lachenmann R and Schultz H 1970 *Scripta Met.* **4** 709
- [53] Duesbery M S and Xu W 1998 *Scripta Mater.* **39** 283
- [54] See for example, Davison L, Grady D E and Shahinpoor M, eds 1986 *High-Pressure Shock Compression of Solids II: Dynamic Fracture and Fragmentation* (New York: Springer-Verlag)
- [55] Barbee T W Jr, Seaman L, Crewdson R and Curran D 1972 *J. of Mater.* **7** 393
- [56] Curran D R, Seaman L and Shockey D A 1987 *Phys. Rep.* **147** 253
- [57] Meyers M A and Aime C T 1977 *Prog. Mater. Sci.* **28** 1
- [58] McClintock F A 1968 *J. Appl. Mech.* **35** 363
- [59] Rice J R and Tracy D M 1969 *J. Mech. Phys. Solids* **17** 201
- [60] Needleman A 1972 *J. Appl. Mech.* **39** 964
- [61] Gurson A L 1977 *J. Eng. Mater. and Tech.* **99** 2
- [62] Belak J 1998 *Shock Compression of Condensed Matter - 1997* AIP Conf. Proc. vol 429, ed Schmidt S C, Dandekar D P and Forbes J W (New York: American Institute of Physics) p. 211
- [63] Belak J 1998 *J. of Comput.-Aided Mater. Design* **5** 193
- [64] Oh D J and Johnson R A 1989 *Atomistic Simulation of Materials: Beyond Pair Potentials*, ed Vitek V and Srolovitz D J (Oxford: Plenum) p. 233
- [65] Belak J and Minich R 1999 *Fracture and Ductile vs. Brittle Behavior - Theory, Modelling and Experiment* MRS Symp. Proc. vol 539, ed by Beltz G E, Selinger R L B, Kim K-S and Marder M P (Warrendale, PA: Materials Research Society) p. 257

- [66] Rudd R E and Belak J 2001 *Comput. Mater. Sci.* in press
- [67] Rudd R E and Belak J 2002 to be published
- [68] Belak J, Rudd R E, Cazamias J, Schwartz A, Kumar M, Minich R, Haupt D and Fivel M C
2001 Lawrence Livermore National Laboratory LDRD initiative 01-ERD-022 unpublished
- [69] Cochran S and Banner D J 1977 *J. Appl. Phys.* **48** 2729
- [70] Abraham F F 1997 *Europhys. Lett.* **38** 103
Abraham F F, Brodbeck D, Rudge W E and Xu X 1997 *J. Mech. and Phys. Solids* **45** 1595
- [71] Zhou S J, Beazley D M, Lomdahl P S, and Holian B L 1997 *Phys. Rev. Lett.* **78** 479
- [72] Kelchner C L, Plimpton S J and Hamilton J C 1998 *Phys. Rev. B* **58** 11085
- [73] Zurek A K and Meyers M A 1986 *High-Pressure Shock Compression of Solids II: Dynamic Fracture and Fragmentation*, ed Davison L, Grady D E and Shahinpoor M (New York: Springer-Verlag) p. 25
- [74] Fivel M C, Robertson C F, Canova G R and Boulanger L 1998 *Acta Mater.* **46** 6183
- [75] Needleman A and van der Giessen E 2001 *Mater. Res. Soc. Bulletin* **26** 211
- [76] Broughton J Q, Bernstein N, Kaxiras E, and Abraham F F 1998 *Phys. Rev. B* **60** 2391
Abraham F F, Broughton J Q, Bernstein N, and Kaxiras E 1998 *Europhys. Lett.* **44** 783
- [77] Rudd R E and Broughton J Q 2000 *Phys. Stat. Sol. (b)* **217** 251
- [78] Rudd R E and Broughton J Q 1998 *Phys. Rev. B* **58** R5893
- [79] Rudd R E 2001 *Advances in Materials Theory and Modeling—Bridging over Multiple Length and Time Scales* MRS Symp. Proc. vol 677, ed Bulatov V, Colombo F, Cleri L, Lewis L and Mousseau N (Warrendale, PA: Materials Research Society) p. AA1.6.1

Figures

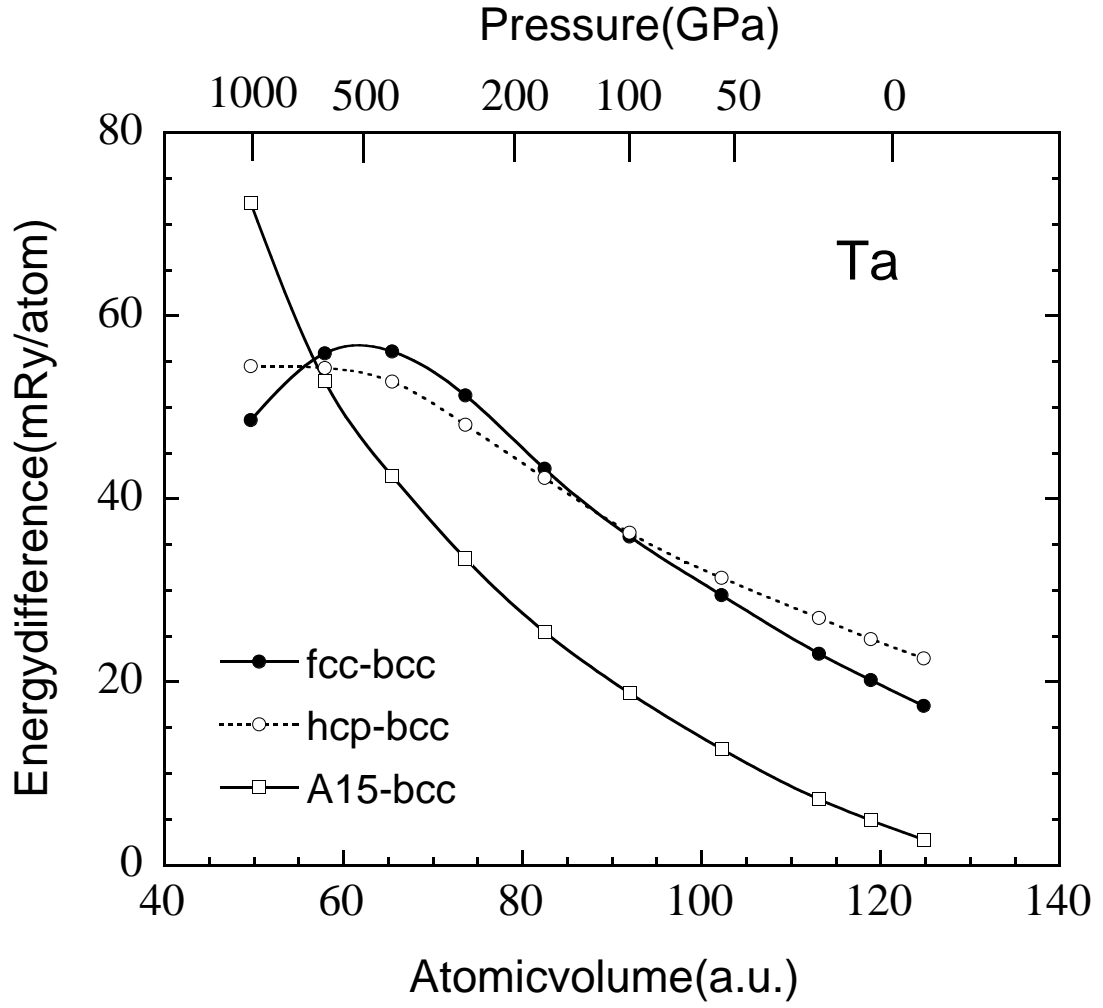


FIG. 1: Predicted structural phase stability in Ta up to 1000 GPa, as obtained from *ab initio* FP-LMTO calculations. Plotted are the zero-temperature total energies of the fcc, hcp, and A15 structures relative to the equilibrium bcc structure.

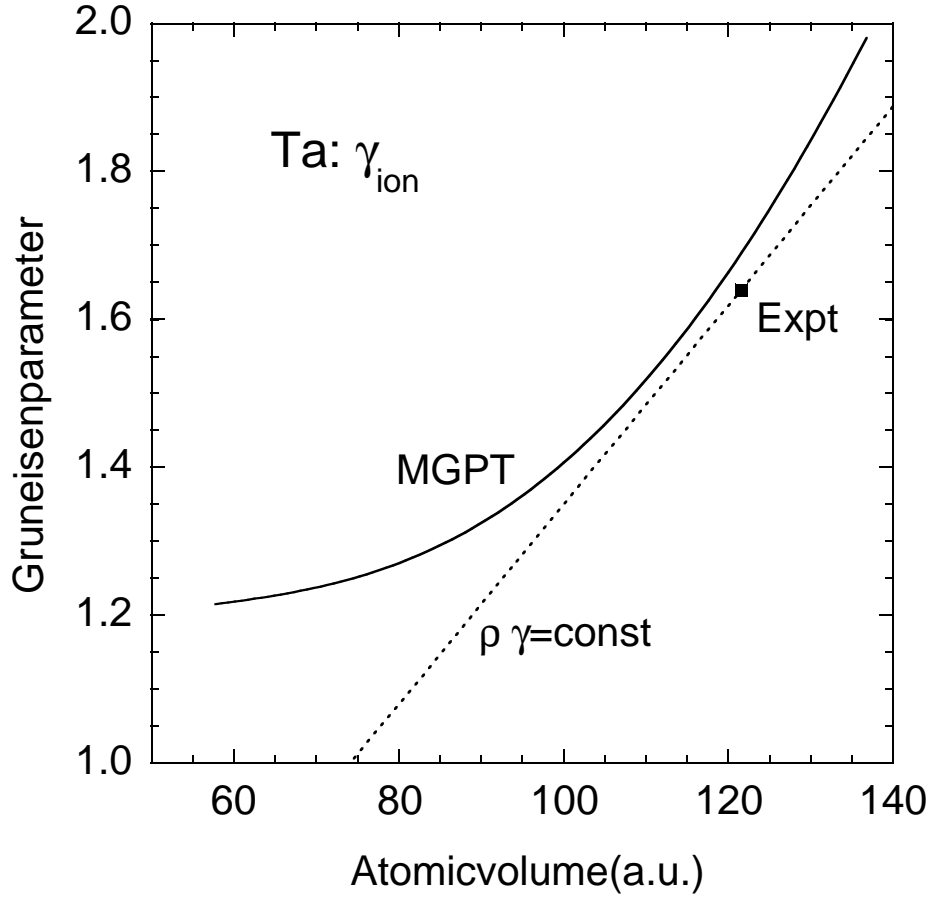


FIG. 2: Volume dependence of the ion-Grüneisen parameter γ_{ion} in Ta, as calculated from MGPT interatomic potentials. For comparison is the experiment value at ambient conditions from Katahara *et al.* [33] and the usual assumed linear variation of γ_{ion} with volume.

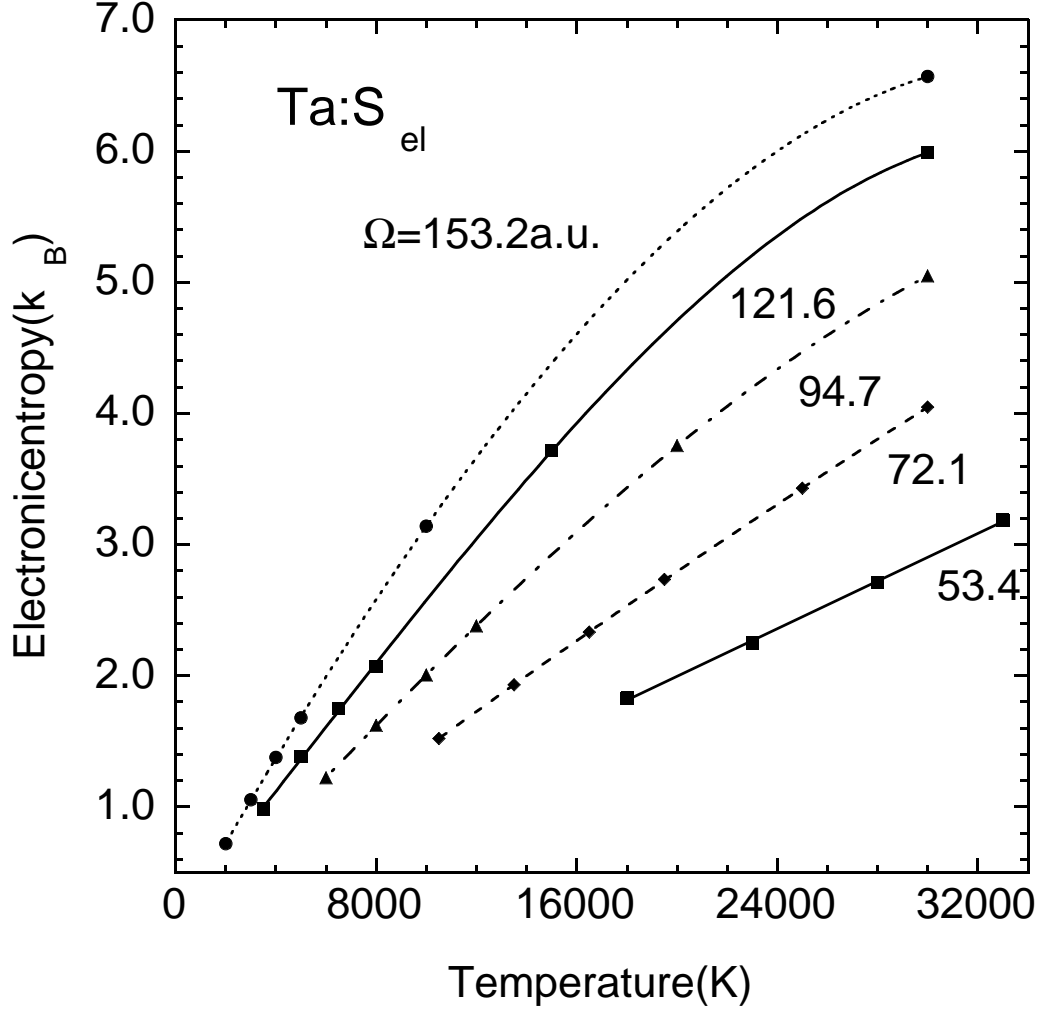


FIG. 3: Predicted electron-thermal component of the entropy in liquid Ta, as obtained from finite-temperature FP-LMTO calculations using snapshot MD/MGPT ion configurations as input and then configuration averaging.

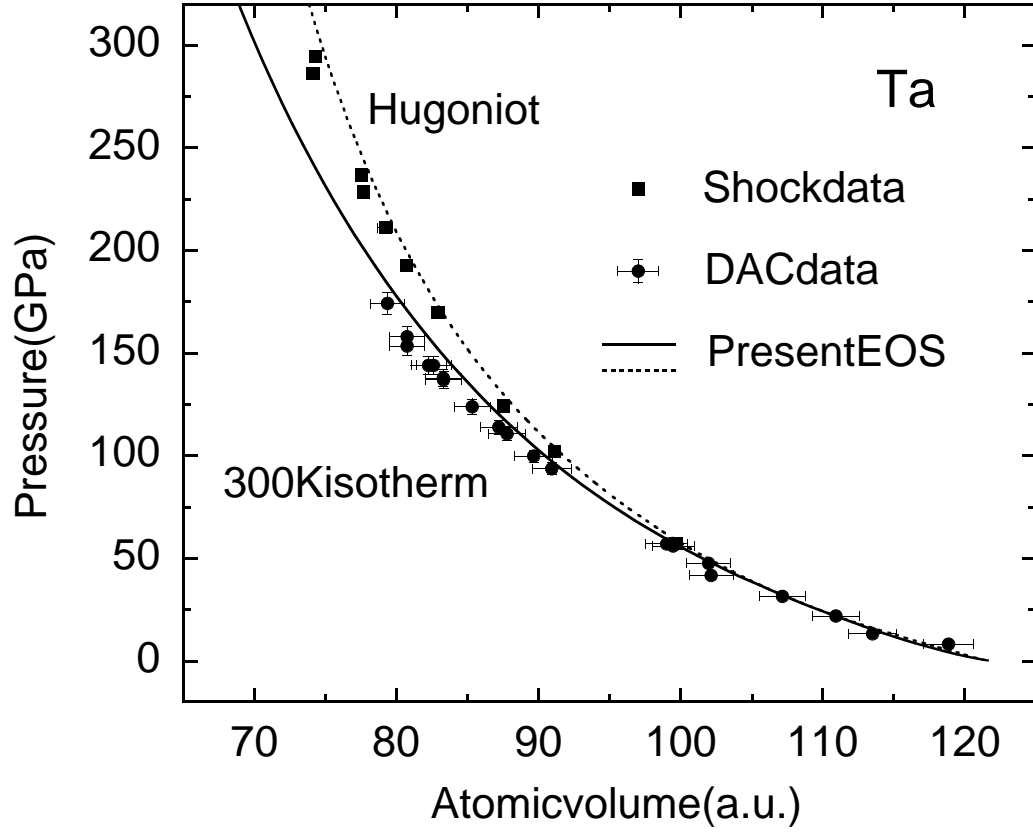


FIG. 4: Room-temperature or 300 K isotherm and principal Hugoniot for Ta, as obtained from the present EOS and as measured in diamond-anvil-cell (DAC) [29] and shock [30] experiments.

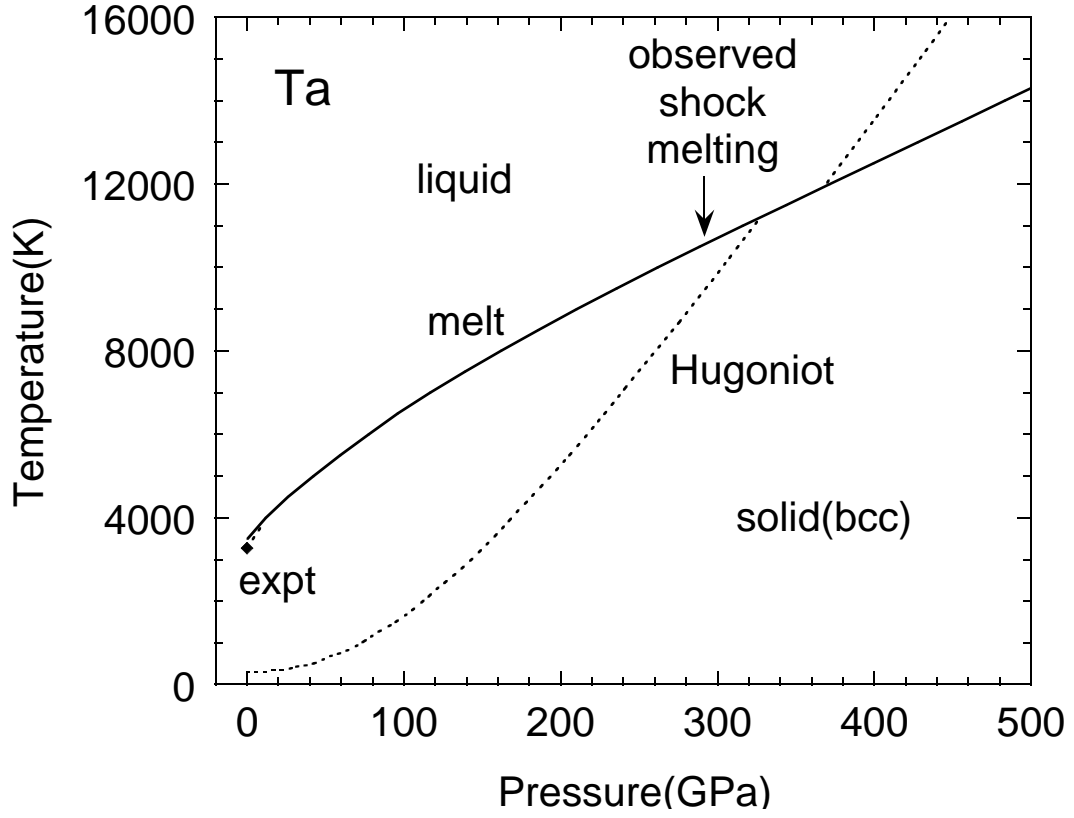


FIG. 5: Equilibrium melt curve (solid line) in Ta, as calculated from the present bcc and liquid free energies discussed in the text. Shown for comparison is the measured ambient-pressure melting point and initial melting slope [35] (solid point and short dotted line). Also shown is the calculated principal Hugoniot (dotted line) and its intersection with the melt curve, which is consistent with the observed onset of shock melting [31] (vertical arrow).

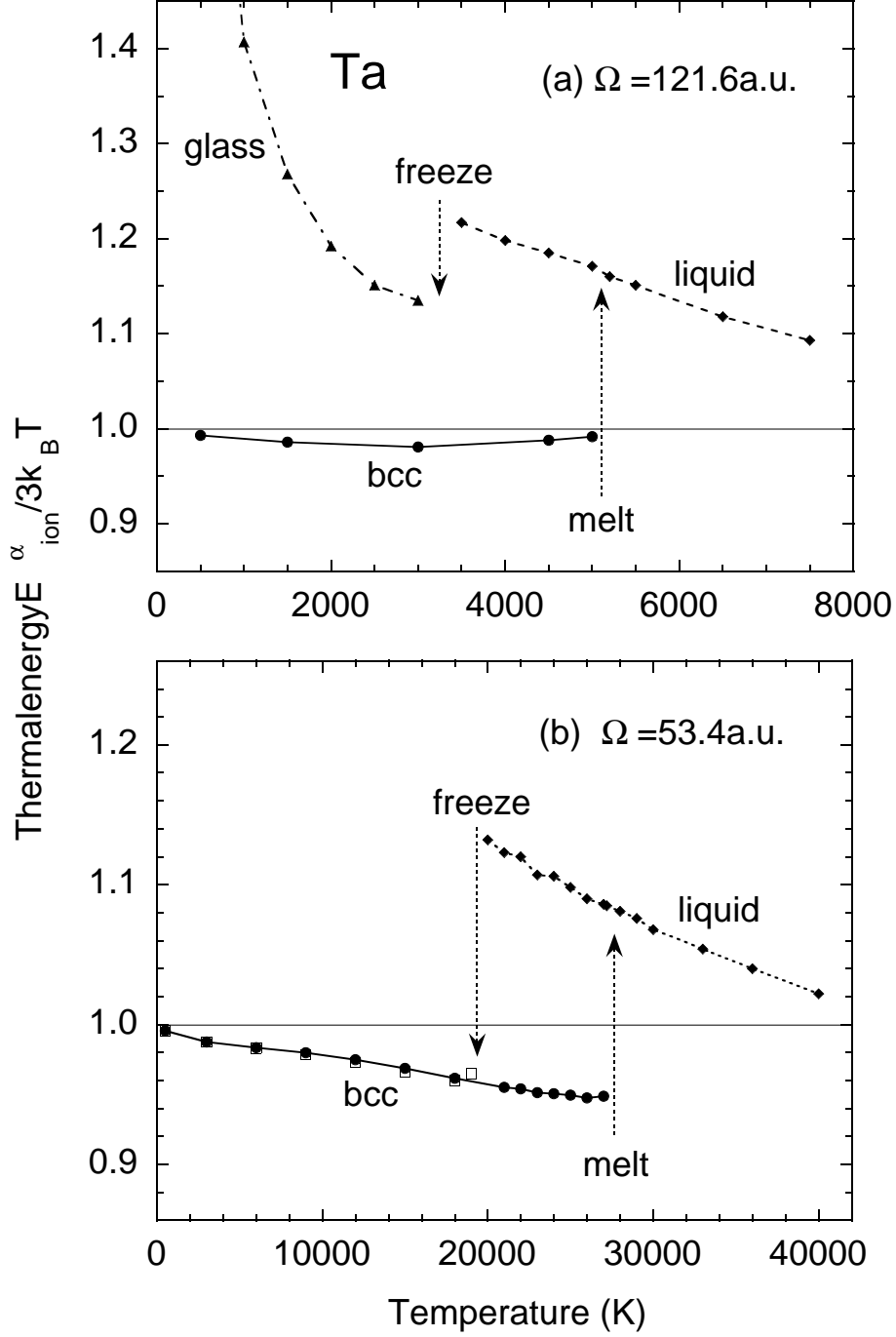


FIG. 6: Relative thermal energies $E_{\text{ion}}^{\alpha} / 3k_B T$ obtained from MD/MGPT simulations in Ta for virgin bcc, melted liquid and resolidified phases in equilibrium under constant-volume conditions. (a) Atomic volume $\Omega = 121.6 \text{ a.u.}$, corresponding to a pressure range of 0-30 GPa, with freezing from the liquid yielding a unique glass structure; (b) Atomic volume $\Omega = 53.4 \text{ a.u.}$, corresponding to a pressure range of 780-1130 GPa, with freezing from the liquid yielding recrystallization into a perfect bcc structure.

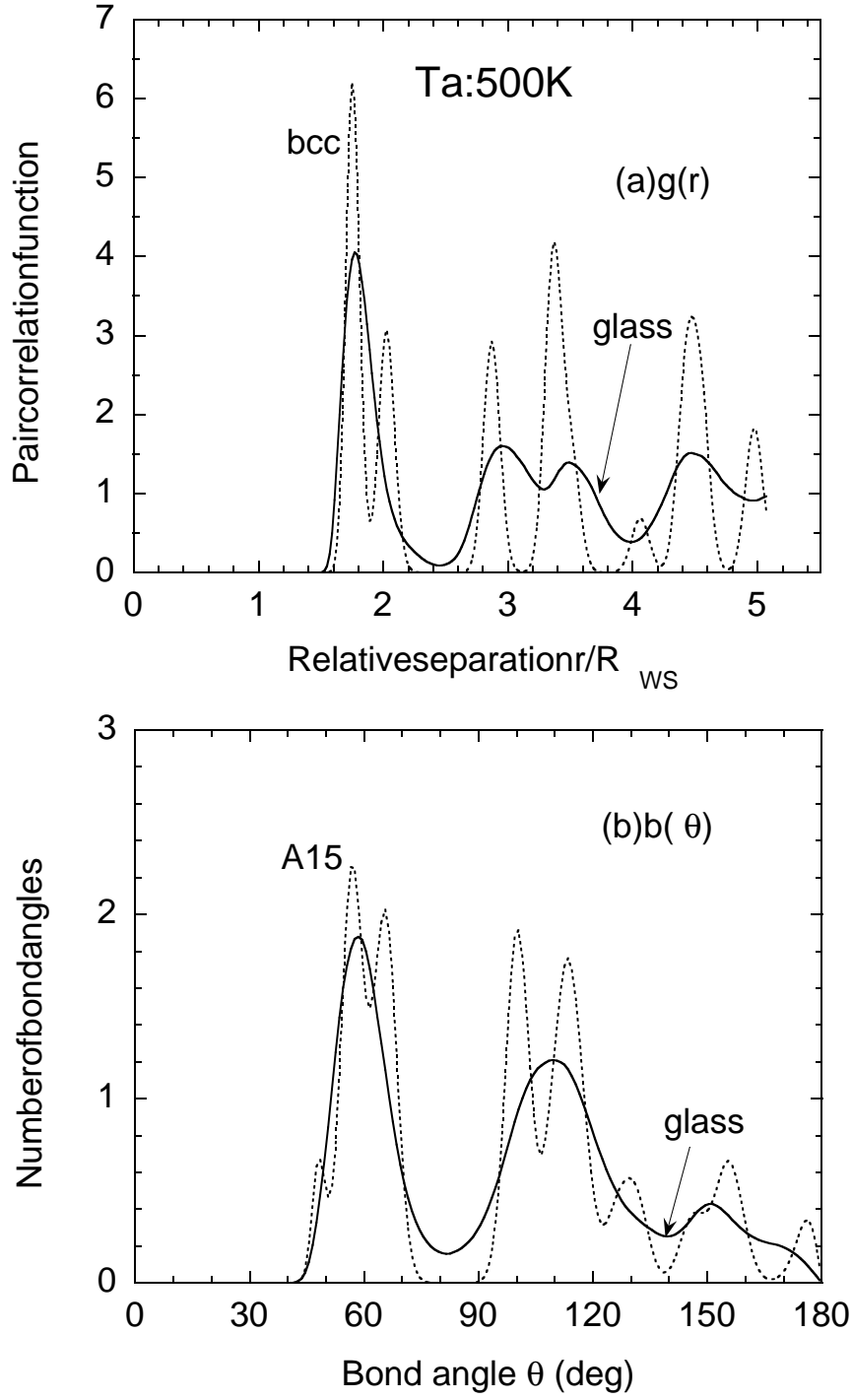


FIG. 7: Radial and angular characteristics of the resolidified glass structure obtained from MD/MGPT simulations in Ta at 500 K and an atomic volume $\Omega = 121.6$ a.u., corresponding to 3.7 GPa in pressure. (a) Pair correlation function $g(r)$ of the glass compared against that of the bcc structure; (b) Angular correlation function $b(\theta)$ of the glass compared against that of A15 structure.

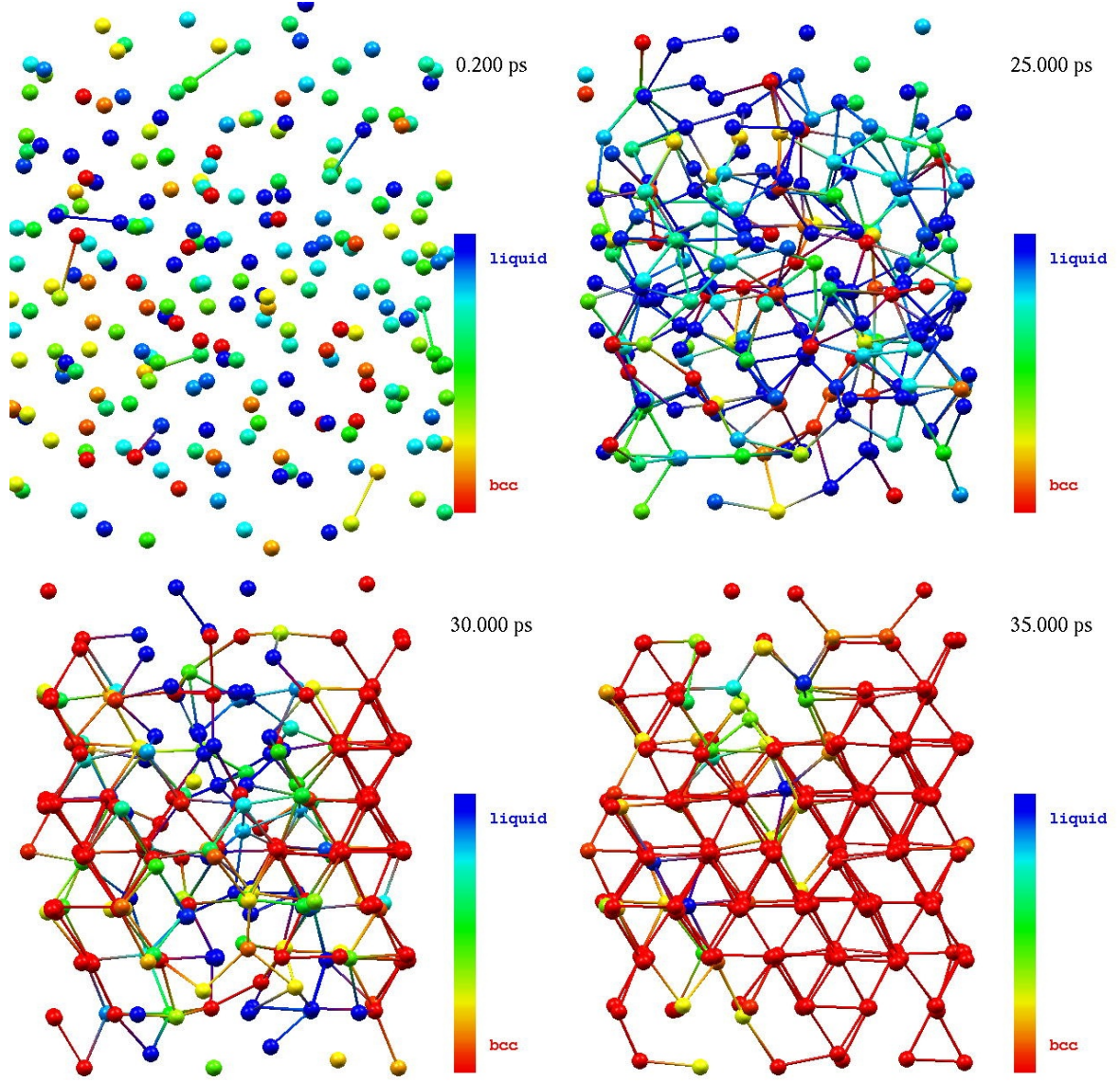


FIG. 8: Temperature and pressure-controlled MD simulation of Ta resolidification under rapid isothermal compression from the melt. A simulation cell of 250 Ta atoms modeled using MGPT potentials has been compressed at 5000 K from near ambient pressure to 300 GPa in about 25 ps. A structural parameter sensitive to the local bonding arrangement has been used to identify atoms in liquid-like and bcc-like environments (shaded blue and red in the snapshots above, respectively). Crystallization into bcc is extremely rapid in this small sample, with virtually complete order attained in the final 10 ps of the simulation near 300 GPa.

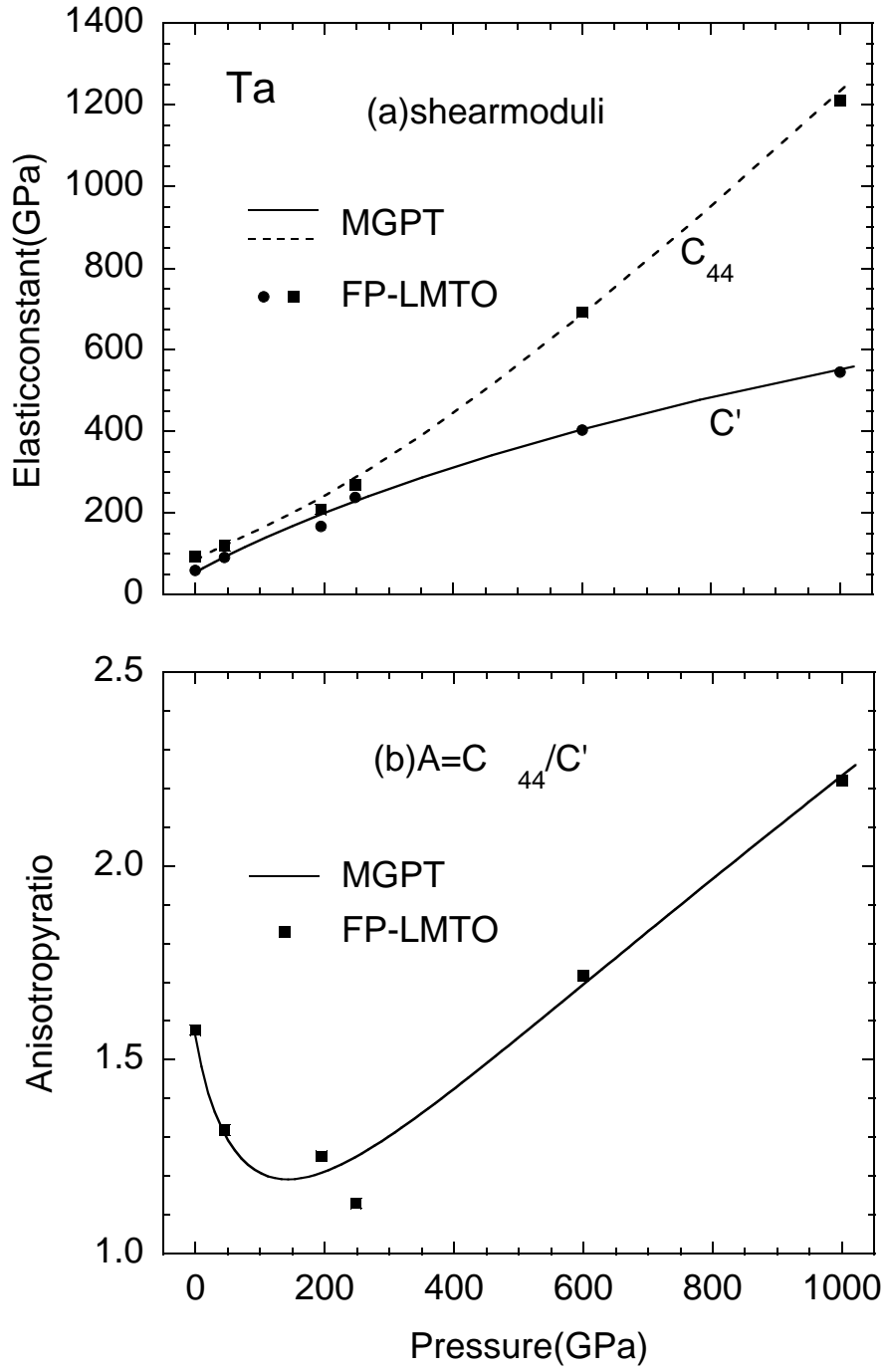


FIG. 9: Pressure dependence of the elasticity in bcc Ta, as obtained from MGPT interatomic potentials and constraining FP-LMTO electronic-structure calculations. (a) Shear moduli C_{44} and C' ; (b) Anisotropy ratio $A = C_{44}/C'$.

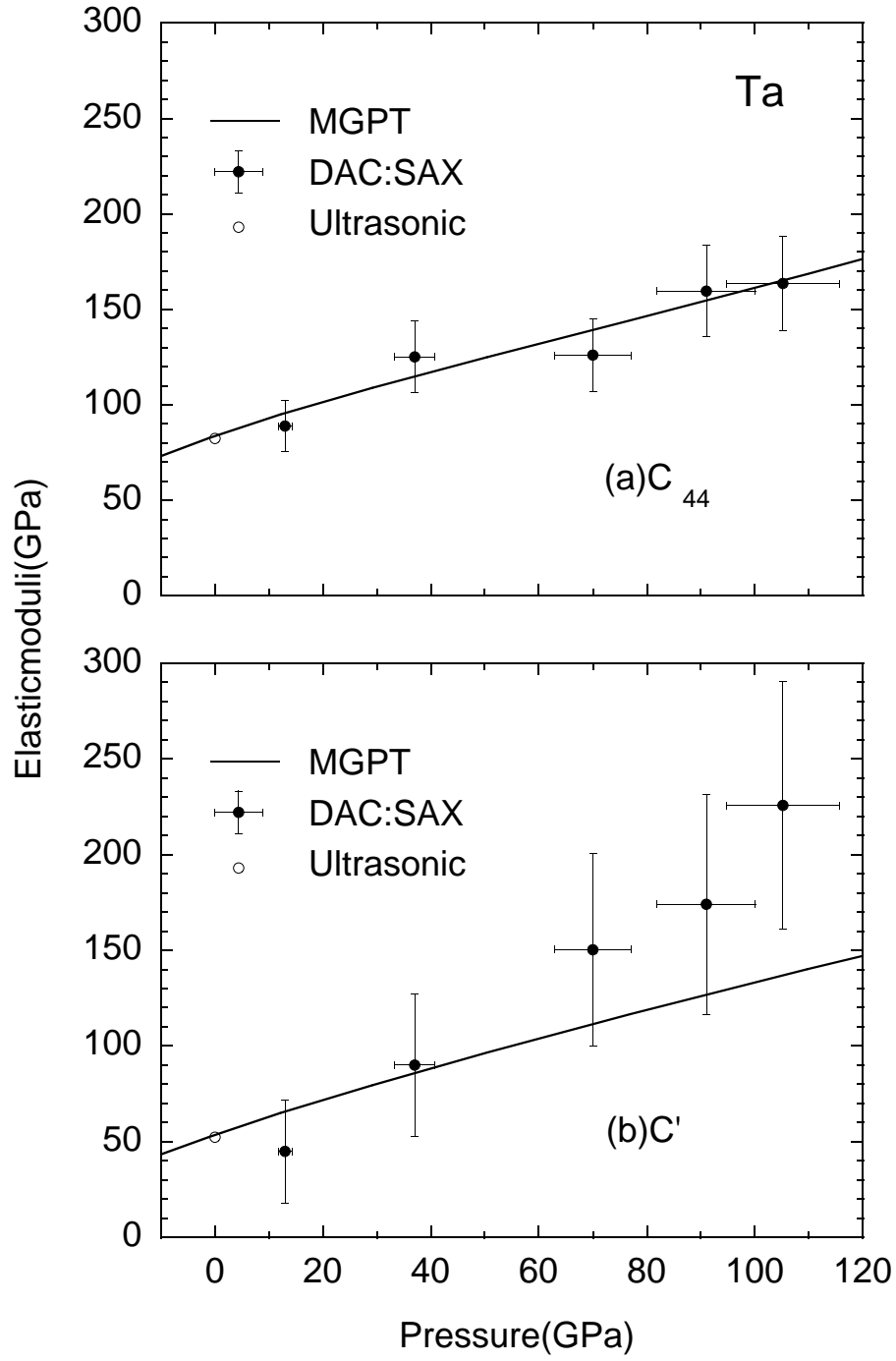


FIG. 10: Comparison of calculated MGPT shear elastic moduli in bcc Ta with measurements in the diamond-anvil cell (DAC) by the SAX technique to about 100 GPa [39] and with ultrasonic data at ambient pressure [33]. (a) C_{44} ; (b) C' .

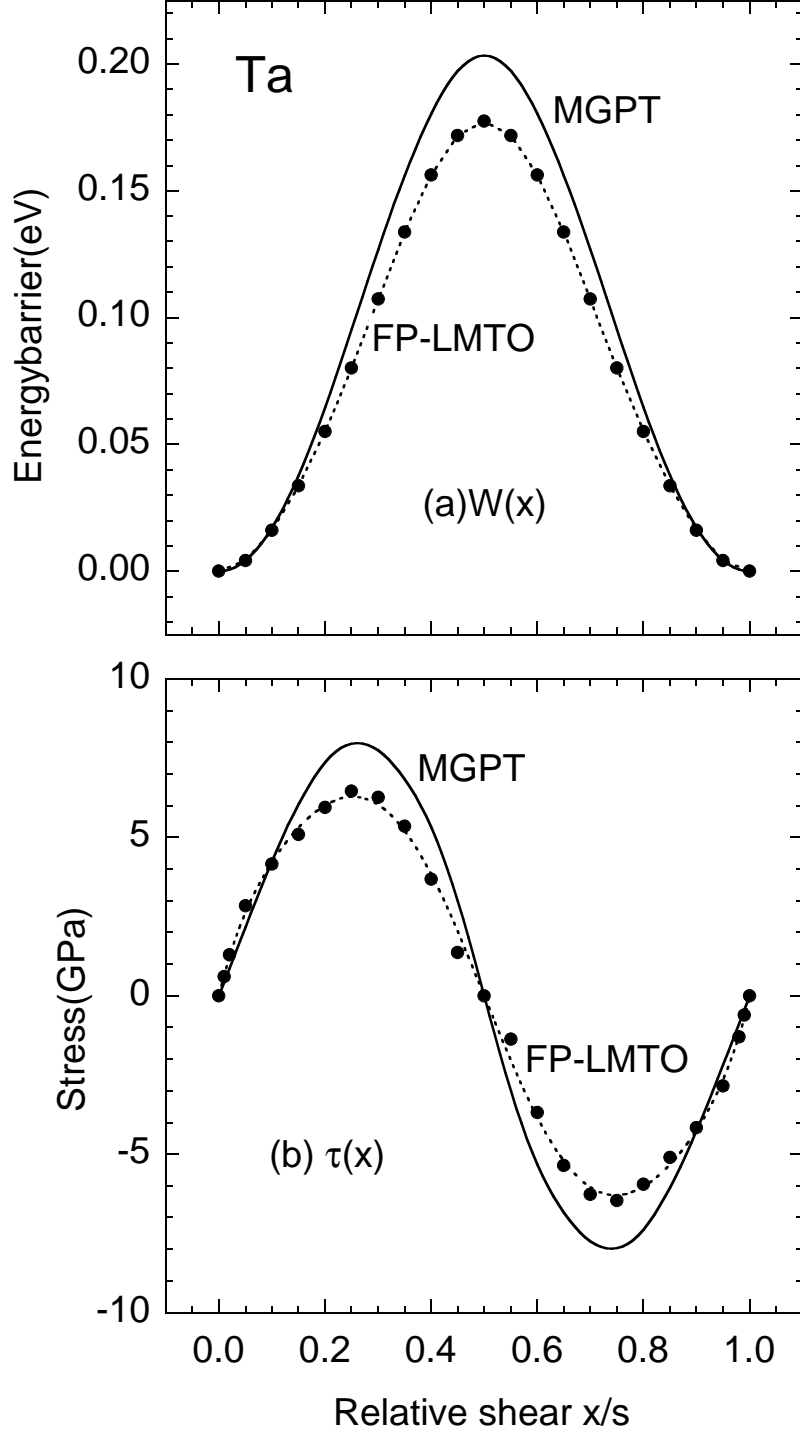


FIG. 11: Unrelaxed ideal shear strength in bcc Ta, as calculated with the *ab initio* FP-LMTO electronic-structure method and with MGPT interatomic potentials. (a) Energy barrier $W(x)$ along the prescribed $(112)/[\bar{1}\bar{1}1]$ twinning path; (b) corresponding shear stress $\tau(x)$ along the same path.

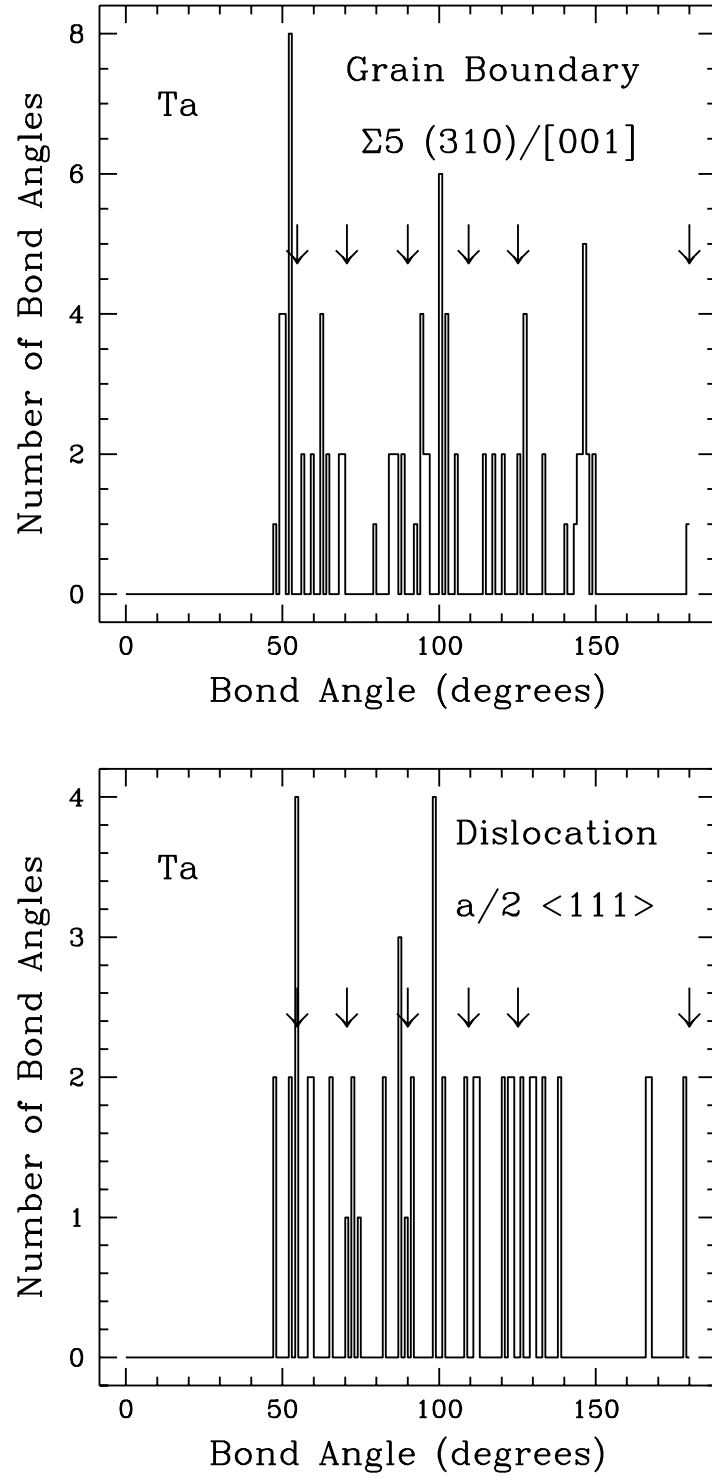


FIG. 12: Distribution of bond angles for near neighbors in the $\Sigma 5$ (310)/[001] symmetric tilt grain boundary (top panel) and in the $a/2$ <111> screw dislocation core (bottom panel) of Ta. The vertical arrows indicate the corresponding bond angles in the perfect bcc lattice.

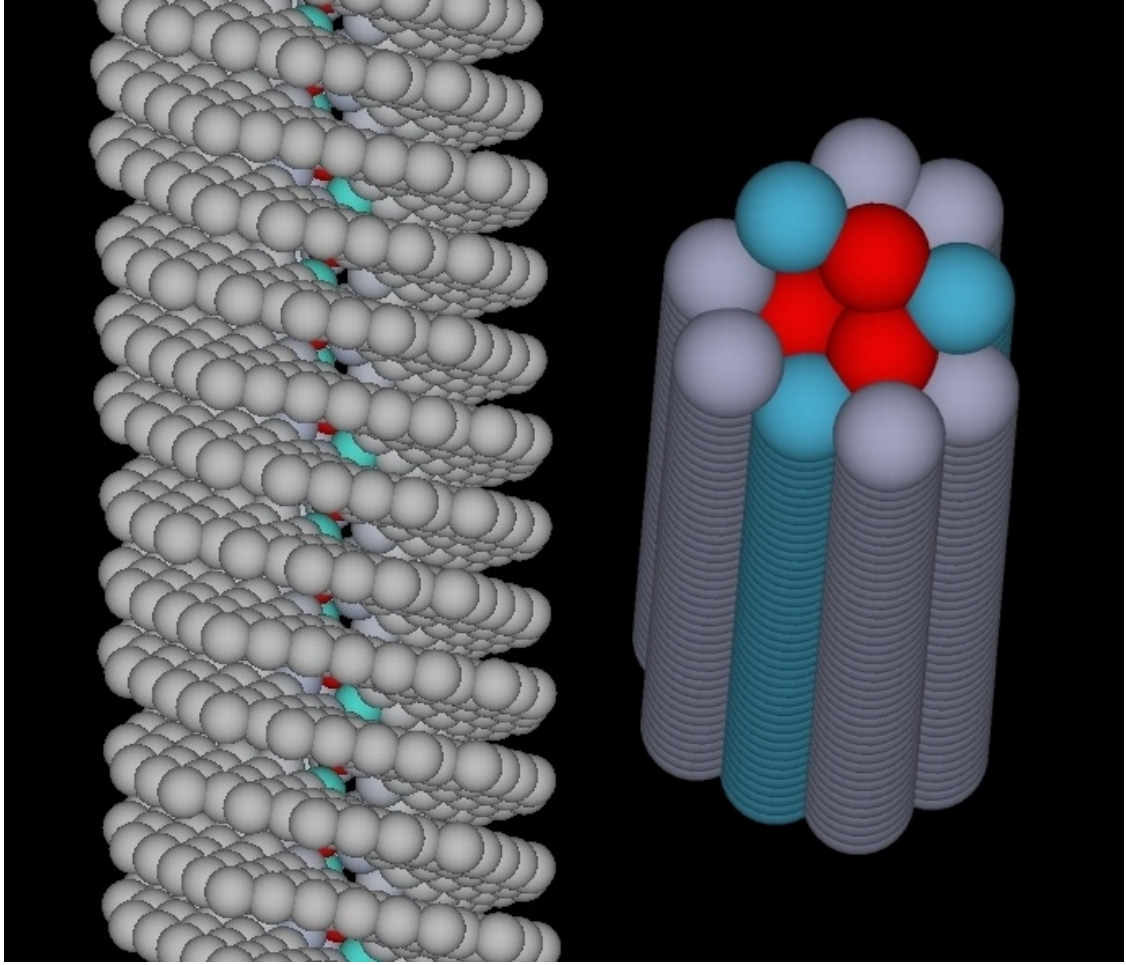


FIG. 13: Two different views of the same $a/2 \langle 111 \rangle$ screw dislocation in Ta. The left image shows the region around the dislocation core stretched 10x along the screw axis in order to visualize the helical nature of the crystal lattice around the core. The right image shows those atoms in the core: the first two shells (the red and blue atoms) are within the equilibrium core radius of 5 Å and the third shell (the gray atoms) is just outside. The atoms are colored according to the amount of local lattice distortion, using the structural characterization scheme discussed in section 5 of the text.

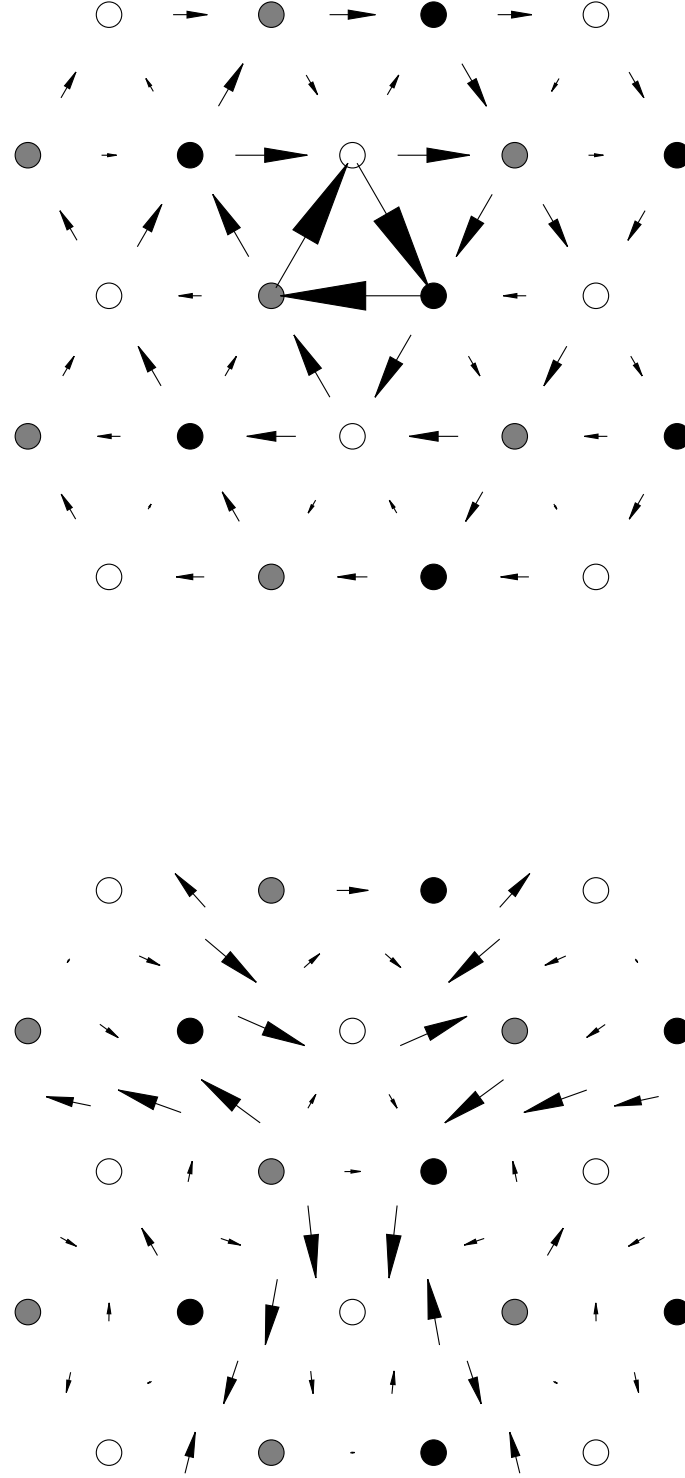


FIG. 14: Core structure of the $a/2 \langle 111 \rangle$ screw dislocation in bcc Ta, as obtained with MGPT interatomic potentials. Top panel: differential displacement map of the screw components of the core; bottom panel: corresponding map of the edge components, magnified by a factor of 10.

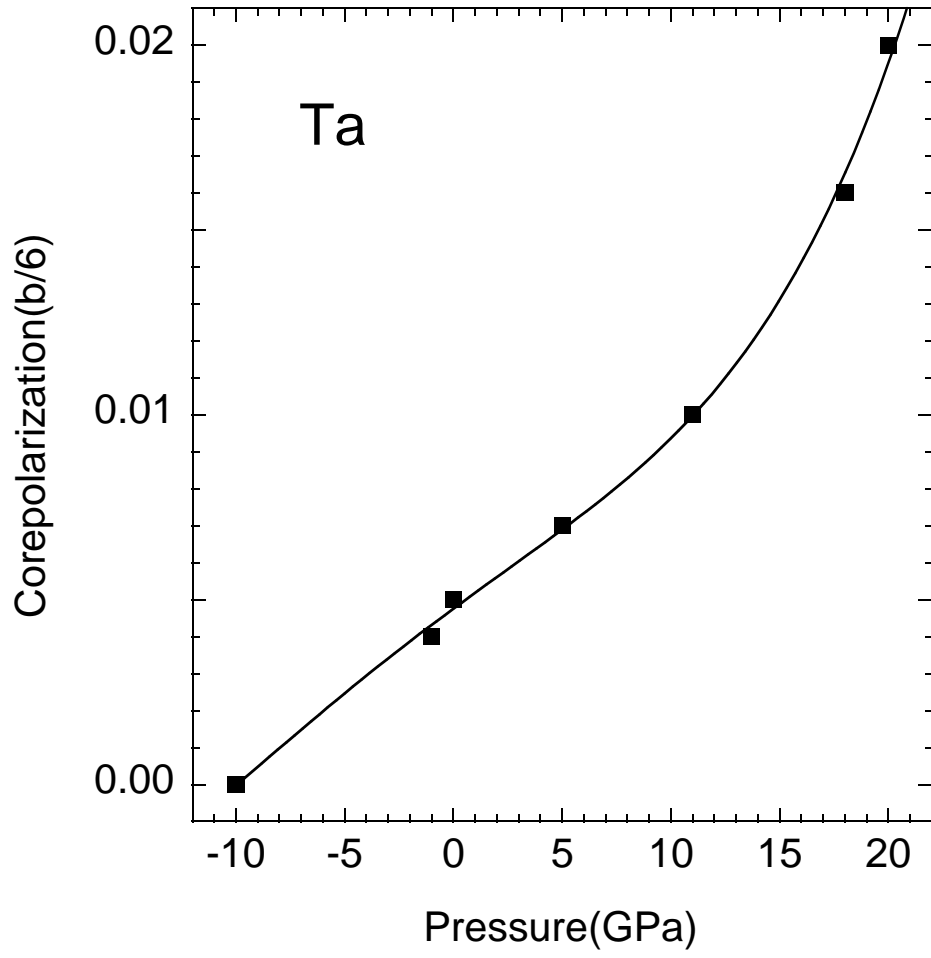


FIG. 15: Pressure dependence of the $a/2$ $\langle 111 \rangle$ screw dislocation core polarization in bcc Ta, as calculated from MGPT interatomic potentials (solid points). The solid curve is a polynomial fit to the calculated points.

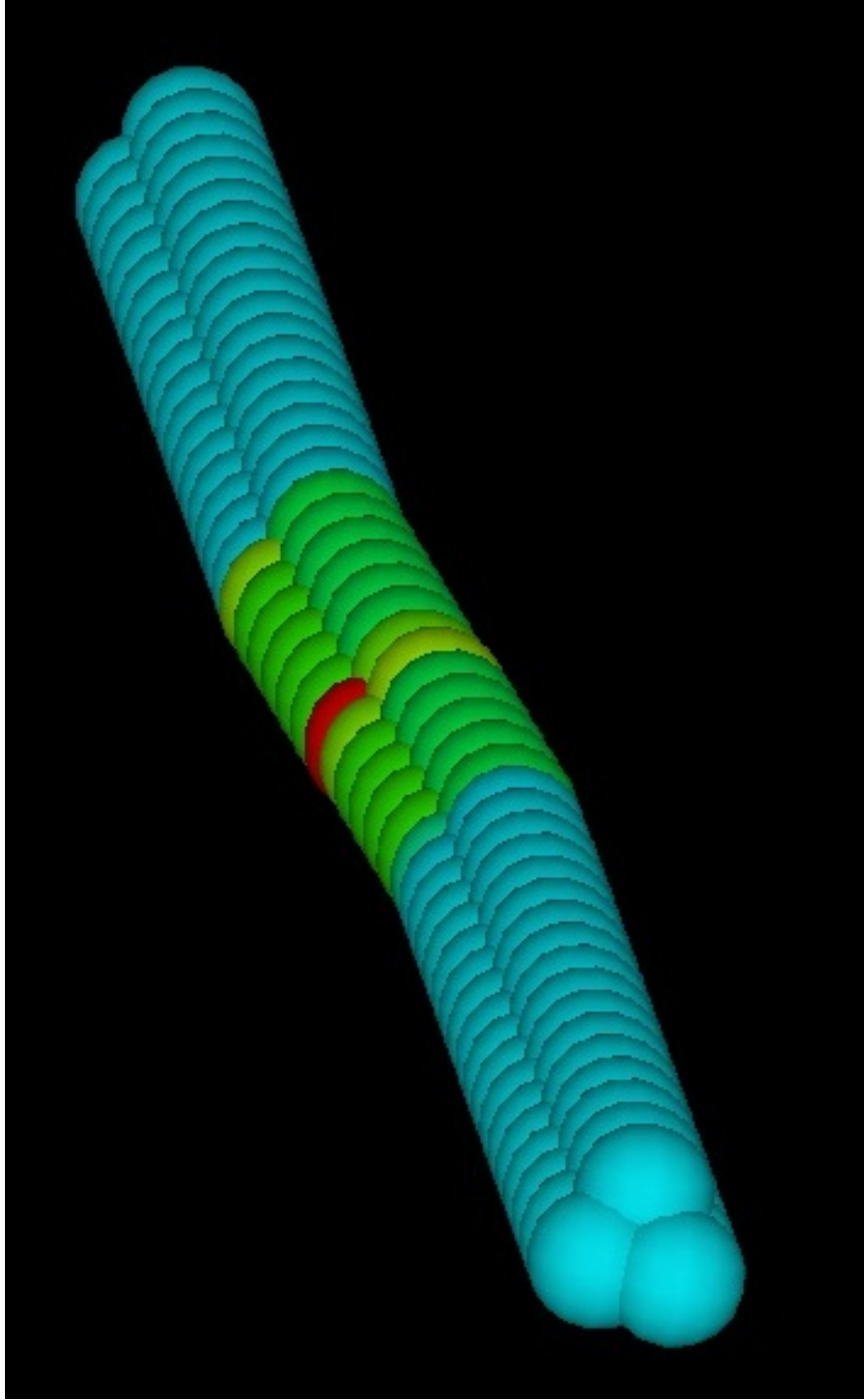


FIG. 16: The central core of the lowest-energy left screw dislocation kink in bcc Ta. The atoms are colored according to the amount of local lattice distortion such that red indicates the greatest distortion and blue the least, using the structural characterization scheme discussed in section 5 of the text.

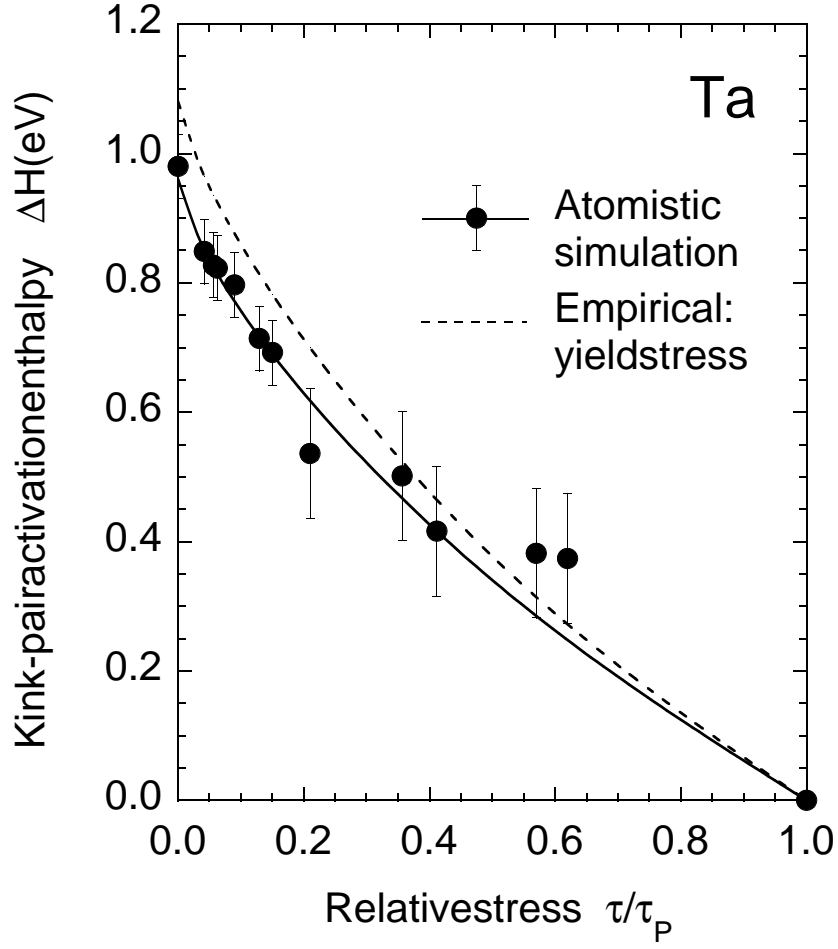


FIG. 17: Activation enthalpy ΔH as a function of relative applied stress τ/τ_p for bcc Ta. The solid line is a fit to the calculated MGPT/GFBC atomistic data (solid points) of the analytic form currently used in dislocation-dynamics (DD) simulations of Ta plasticity. The dashed line is the empirical DD result from Tang *et al.* [50] based on the observed single-crystal yield stress.

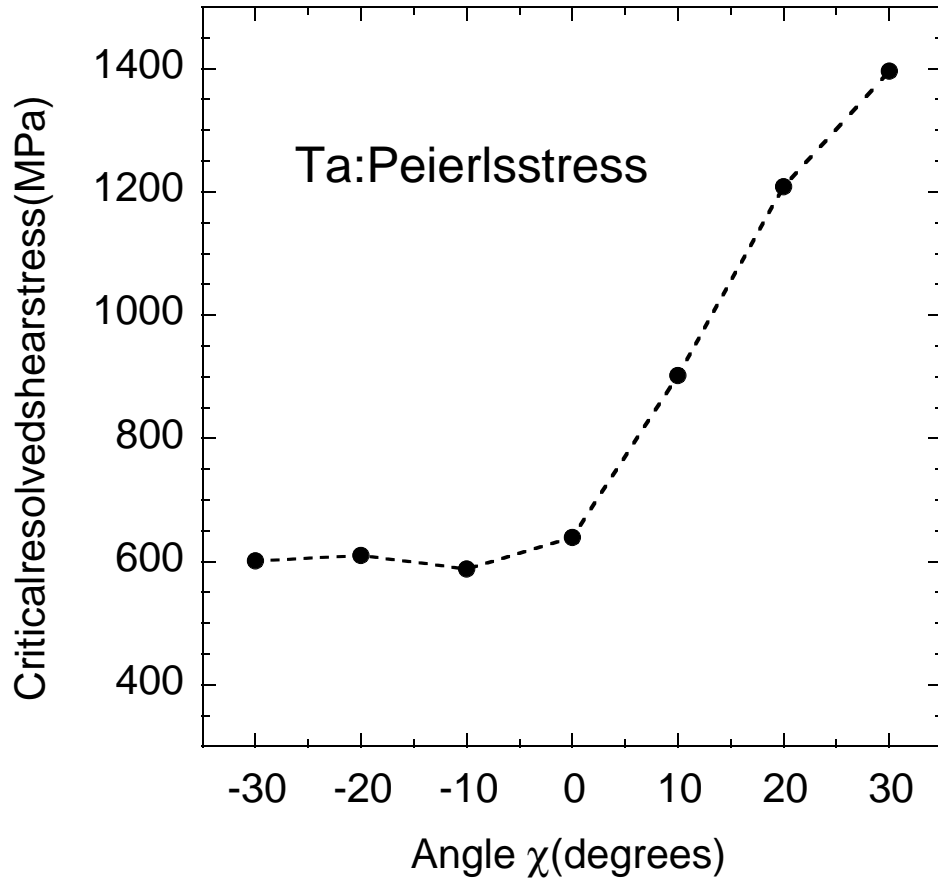


FIG. 18: Calculated orientation dependence of the critical resolved shear stress for a rigid $a/2$ $\langle 111 \rangle$ screw dislocation in bcc Ta, as obtained with MGPT interatomic potentials for pure shear loading.

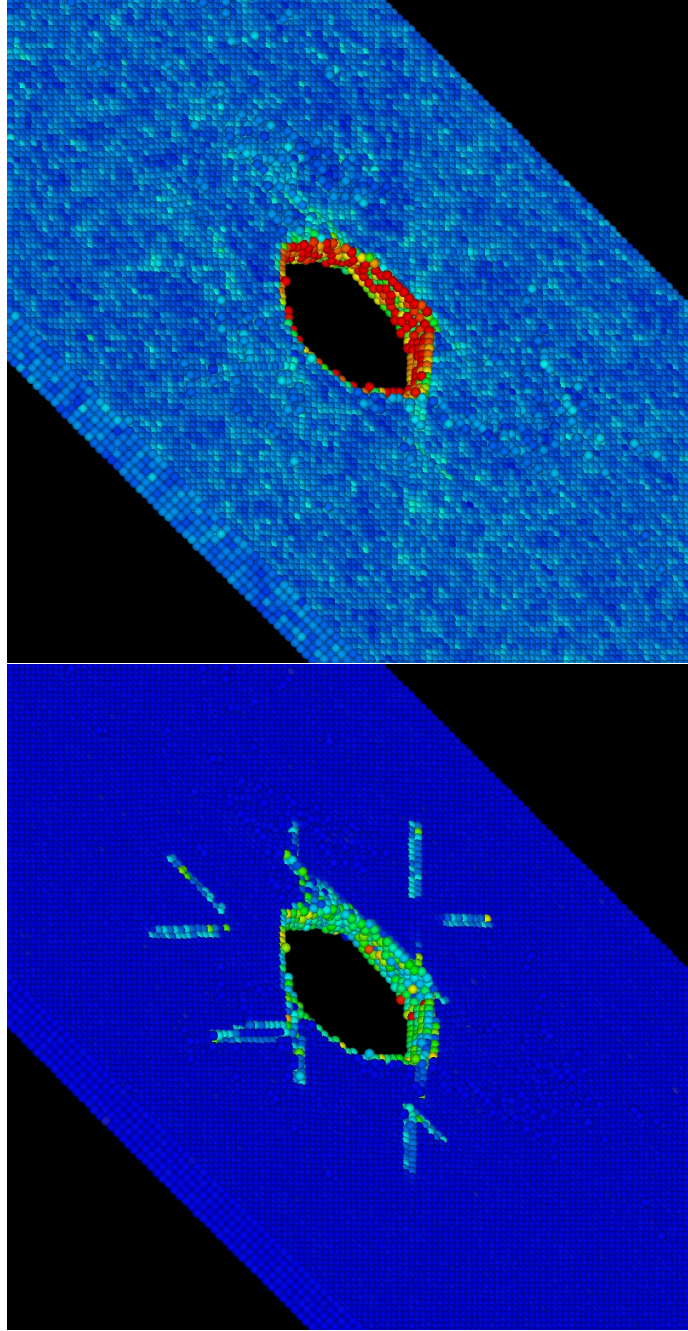


FIG. 19: A 2D slice of a growing void simulated in Cu at room temperature and shown at a point where the simulation cell has expanded 1.3% and the initially spherical void has grown by 44% in each direction. This slice is the (111) plane through the center of the void. The top panel shows the atoms colored according to their energy, and the dislocation structure is indistinguishable from thermal fluctuations. The bottom panel shows the atoms colored according to a structural symmetry-deviation parameter (see text). The dislocations are clearly identified by this parameter.

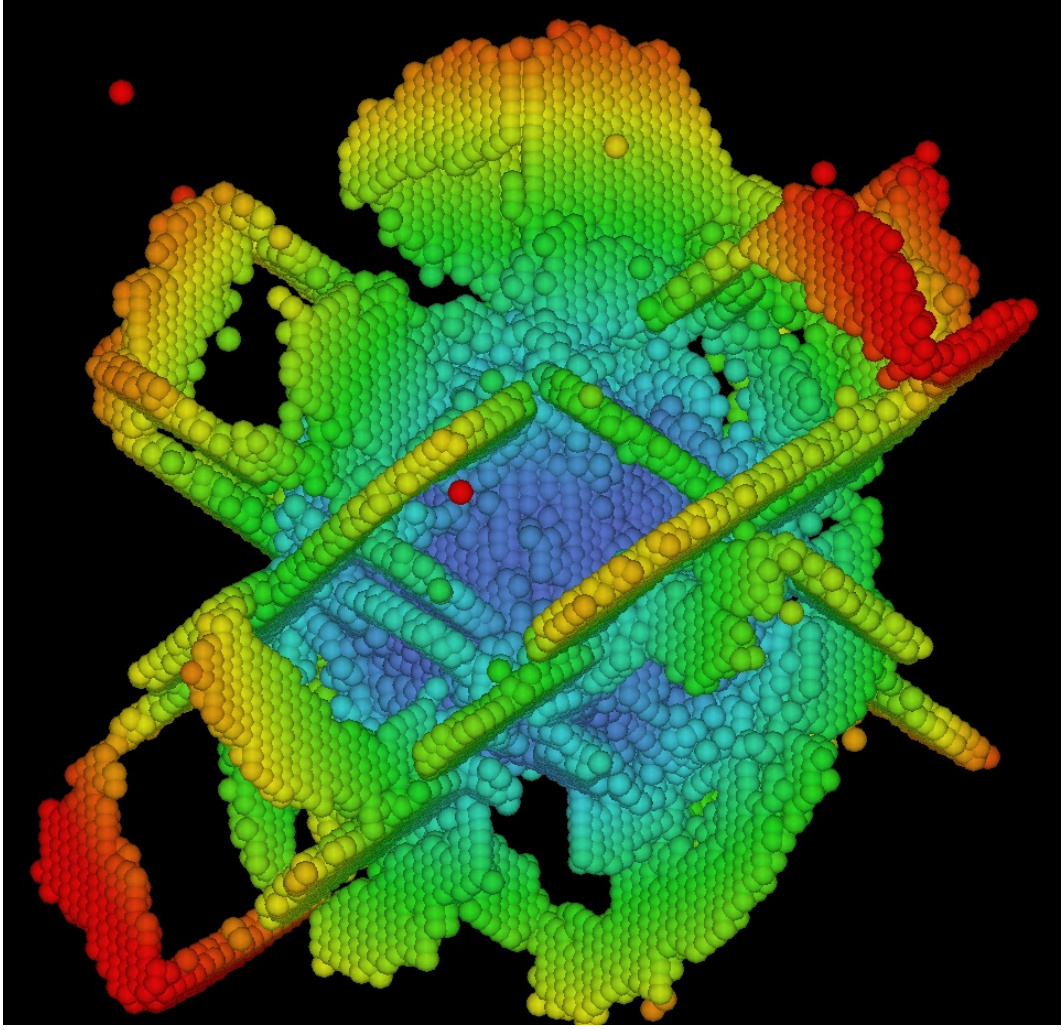


FIG. 20: The figure shows prismatic loops punched out in the simulation of the growth of a spherical void in single-crystal Cu at room temperature. The spheres represent individual atoms. Only atoms participating in the void surface, dislocation cores or stacking faults are shown. The color denotes the distance from the center of the void.

Tables

TABLE I: Vacancy and $\langle 110 \rangle$ split-dumbbell self-interstitial formation energies ($E_{\text{vac}}^{\text{f}}$ and $E_{\text{int}}^{\text{f}}$), migration energies ($E_{\text{vac}}^{\text{m}}$ and $E_{\text{int}}^{\text{m}}$), and formation volumes ($\Omega_{\text{vac}}^{\text{f}}$ and $\Omega_{\text{int}}^{\text{f}}$) for bcc Ta. Energies are given in eV.

	$E_{\text{vac}}^{\text{f}}$	$E_{\text{vac}}^{\text{m}}$	$\Omega_{\text{vac}}^{\text{f}}/\Omega_0$	$E_{\text{int}}^{\text{f}}$	$E_{\text{int}}^{\text{m}}$	$\Omega_{\text{int}}^{\text{f}}/\Omega_0$
MGPT	3.08	0.78	0.51	6.37	0.50	0.4
PP	3.10	0.90	0.60	6.65	0.60	0.2
FP-LMTO	3.10	0.74				
Experiment ^a	2.8-3.1	0.7				

^aFrom [41]

TABLE II: Atomic structure of the $\Sigma 5$ (310)/[001] grain boundary in bcc transition metals, as predicted from MGPT interatomic potentials and as measured in HREM experiments. Displacements in units of the bulk lattice constant a_0 .

Metal	Mirror Symmetry		[001] Displacement	
	MGPT	HREM	MGPT	HREM
Nb ^a	Yes	Yes	0.0	0.0
Mo ^b	No	No	0.2	0.25±0.05
Ta ^c	No	No	0.17	0.17±0.05

^aFrom [42]

^bFrom [43]

^cFrom [44]

[illegible]